THE FLORIDA STATE UNIVERSITY

COLLEGE OF ARTS AND SCIENCES

ON THE DYNAMICAL RESPONSE OF THE SUBARCTIC FRONT TO MOMENTUM TRANSFER

by

ALEJANDRO CAMERLENGO

A Dissertation submitted to
the Department of Meteorology
in partial fulfillment of the
requirements for the degree of
Doctor of Philosophy

Approved:

James J. O'Brien
Professor Directing Dissertation

March, 1981

A Alejandra y al

Pueblo de Nicaragua

ABSTRACT

Theoretical studies and numerical experiments of the subarctic front are conducted. The theoretical side of this research encompasses the determination of a stability criterion and the role friction plays as a dissipative mechanism. In the first case study, it is established that if the difference between the phase speed of the perturbation and the mean long-front geostrophic flow is greater than a certain value, the subarctic front is stable everywhere. In the other case study, it is proved that the time scale of dissipation is sufficiently large to neglect horizontal friction. While the effect of the westerly winds causes a southward shift of the front, the effect of a negative curl shows convergence at the front. This convergence strongly favors frontogenesis.

It is established that the phase speed of the first baroclinic mode is larger in a numerical model where a constant density jump between layers is employed. Thus, a smaller time scale is required to avoid the numerical instability caused by the violation of the CFL criterion. A numerical four-layer hydrodynamical model is implemented to investigate the role the atmosphere exerts on the dynamics of the subarctic front.

The salient features at the wake of a strong cyclone can be summarized as follows: (i) upwelling of 20 meters of the four interfaces occurs; (ii) the water remains upwelled for several weeks; (iii) the e-folding time scale of the vertical oscillations induced by the storm's
occurs; (ii) the water remains upwelled for several weeks; (iii) the e-folding time scale of the vertical oscillations induced by the storm's
passage is of the order of 10 days; (iv) a region of relative maximum

convergence is observed in the lower layers below a region of relative maximum upwelling in the upper layer; and (v) the long and cross-front velocity fields are in quadrature in time, with the cross front velocity lagging the long front velocity.

With the exception of the cyclone's case, it is established that the effects of the atmospheric wind forcing are confined to the upper layer. These results are supported by oceanic observations. Finally, it is also proved that the response of the front to the atmospheric momentum transfer is independent of the initial form of the subarctic front.

ACKNOWLEDGMENTS

This research was supported by the Office of Naval Research, Ocean Science and Technology Branch, under contract N000-14-80-C0076. Computations were performed on the CDC Cyber 74 at Florida State University, Tallahassee, Florida.

I wish to express my gratitude to Dr. James J. O'Brien, my major professor and thesis advisor. He inspired me throughout my graduate career and taught me the fundamentals of numerical modelling. I also wish to thank him for his encouragement, support and helpful suggestions during the course of this research. I also wish to extend my appreciation to Drs. Albert Barcilon, Noel LaSeur, Thomas Gleeson and Eutiquio Young for serving as members of my doctoral committee.

To Dr. Benoit Roisin I wish to express my appreciation for reading the manuscript and for many hours of enlightening discussions. Also, I wish to extend my thanks to Mr. James Merritt whose help was vital to the solution of many computer system problems. The facilities provided by Dr. Tony Sturges are also very much appreciated.

I would like to acknowledge the assistance of Mrs. Ruth Pryor, Mrs. Sheila O'Brien and Mr. Dewey Rudd. All the draft copies and the final version of this research were typed by Ms. Pat Heaton to whom I am very grateful.

LIST OF TABLES

LIST OF ILLUSTRATIONS

First cyclonic case after 6 days.

Fig. 8. Same as Fig. 7 but after 15 days.

Fig. 17. Isoanomalies of the height field of the upper layer of the undulatory front for the case of the cyclone travelling from west to east after 10 days.

TABLE OF CONTENTS

REFERENCES 90

1. INTRODUCTION

The aim of this investigation is to contribute to the understanding of the dynamics of large-scale upper oceanic fronts, with particular emphasis on the subarctic front of the North Pacific. Although this study is primarily intended to be a numerical one, theoretical aspects such as the stability and the determination of the time scale of dissipation due to horizontal friction of oceanic fronts also have been addressed.

The literature related to oceanic fronts is modest while the literature of atmospheric fronts is quite vast and profuse. The first attempts in the understanding and the physical interpretation of atmospheric fronts began early in this century. The classical Norwegian school was the first which attempted to understand this meteorological phenomenon. The papers of Bjerknes (1919) and Bergeron (1928) are classical in this matter.

More comprehensive studies of atmospheric fronts showed the inadequacy of the classical Norwegian frontal point of view. The study of Sanders (1955) showed the evidence of a new type of front: the surface front. The intensity of this frontal zone is much greater at the surface than at higher levels in terms of horizontal gradients of both wind and temperature.

The papers of Reed and Sanders (1953) and Reed (1955) draw attention to another type of frontogenetical phenomenon: the upper tropospheric

The papers of Reed and Sanders (1953) and Reed (1955) draw attention to another type of frontogenetical phenomenon: the upper tropospheric front.

The papers of Hoskins (1971), Hoskins (1972) and Hoskins and Bretherton (1972) should be interpreted as a way to simulate numerically these two fronts. They achieved moderate success with their numerical simulations by making numerous assumptions: Boussinesq approximation; geostrophic balance across but not along the front; rigid lid approximation; omission of the curvature terms; f-plane approximation; and unrealistic deformation field which cannot be valid in the whole troposphere. In their simulation of surface fronts, there were three salient features: intense convergence at the surface front and a strong upward motion above it; in the warmer air there was a tendency to move upward along the isentrops, while in the cold air there was a tendency to subside; after a certain time the numerical solutions showed infinite vertical vorticity at the surface. On the other side of the spectrum, their simulation of the upper tropospheric front showed a remarkable discontinuity between tropospheric and stratospheric air. Hoskins and Bretherton were successful enough in simulating the folding of the tropopause, but only down to 400 mb. Because of the Boussinesq approximation, the vertical displacements were limited. Nevertheless, when non-Boussinesq effects were included, Hoskins obtained only slightly better results. Unfortunately, the main discrepancies remain unaltered.

In a numerical study, Shapiro (1975) implemented a 20-level isentropic coordinate primitive equation in order to simulate upper level frontogenesis. He was fairly successful in predicting the folding of the tropopause down to a level of 500 mb. The vertical coordinate he used was potential temperature, which allows a vertical variable resolution.
tropopause down to a level of 500 mb. The vertical coordinate he used was potential temperature, which allows a vertical variable resolution.
He based his study on the papers of Eliassen and Raustein (1970), using

their same initial conditions. In our model, although density will be the vertical coordinate, the philosophical approach will be somewhat similar to the isentropic coordinates system proposed by Eliassen and Raustein (1970). Similar studies have been done involving research with models of the ocean, rather than the atmosphere.

Tareyev (1968), using a simple two-layered model, studied the baroclinic instability in the section of the Gulf Stream current between Florida and Cape Hatteras, where the width of the Gulf Stream current is very narrow (approximately 100 km). By neglecting the β-effect and taking into account the non-geostrophic effects, he was able to show that the flow is baroclinically stable in the section of the Gulf Stream current as the internal Froude number is less than one. In this same paper Tareyev explained the contradiction between Kotchin's model and the quasigeostrophic models. In Kotchin's model the baroclinic instability occurs when the vertical velocity shear decreases, while in the latter models the baroclinic instability increases with increasing vertical shear after reaching a critical value.

Orlanski (1968) applied Kotchin's model in an f-plane in order to study the instability of a frontal surface. He found that in the region of Rossby and Richardson numbers less than three, unstable waves exist for all wavelengths. While studying the region of complex eigenvalues, he found a new form of instability at small Richardson numbers: the Rayleigh instability. Abramov, et al. (1972) extended Orlanski's results for a β-plane approximation. Their study reveals that for a fixed Rossby number, baroclinic instability increases rapidly with the Richardson

number and then decreases monotonically. Moreover, for an increasing Richardson number, the region of unstable waves narrows. This study also reveals the destabilizing effects introduced by the beta effect at certain wavelengths. In all quasigeostrophic models which do not consider the latitudinal dependence of the variables of the basic state, the beta effect has a stabilizing effect.

The study and understanding of oceanic fronts is in its infancy as compared with that of atmospheric fronts. There are two powerful reasons which account for this phenomenon. While an enormous amount of meteorological data is obtained from the atmosphere on a daily basis, it is much more costly and difficult to obtain accurate data from the ocean. Another reason is that in the atmosphere at a certain pressure level, the density and the temperature fields are inversely related, via the equation of state.

The picture is completely different in the ocean. Another parameter is present in the equation of state: salinity. In oceanography, each field will have to be studied separately, and it is proper to individualize each one of them. Finally, semantic difficulties arise from the fact that oceanic fronts exist on numerous space and time scales. Thus, they are governed by different dynamics, characterized by different properties and driven by different forces.

When the temperature and salinity fronts happen to compensate each other, the density front is very weak. The oceanic subarctic front typifies this case (Roden, 1972). In an opposite sense, in the case of the subtropical front, the density front is more pronounced because the

typifies this case (Roden, 1972). In an opposite sense, in the case of the subtropical front, the density front is more pronounced because the temperature and the salinity front do not tend to compensate each other.

Hoskins and Bretherton (1972) noted that there are at least eight mechanisms important in changing temperature gradients and forming atmospheric fronts: 1) horizontal deformation field, 2) horizontal shear mechanism, 3) vertical deformation field, 4) differential vertical motion, 5) latent heat release, 6) surface friction, 7) mixing processes, and 8) radiation. In the ocean, the first six mechanisms can be important; the last two are negligible. For the purpose of oceanic frontogenesis, horizontally non-uniform buoyancy fluxes (heating and cooling, precipitation and evaporation, river run-off, ice melt, ice brine, etc.) may also be considered.

Bleck (1978) simulated coastal upwelling frontogenesis on a β-plane using a Lagrangian type of formulation. In his study he handled the serious problem of the intersection of the interface with the sea surface by using a new technique: the "hole-filling technique." This technique constitutes no more nor less than a different way of smoothing. Clearly, "hole-filling" is not the answer to the problem.

Garvine (1974) developed a non-rotating model of small-scale oceanic fronts. His study revealed that interfacial friction must balance the horizontal pressure produced by the sloping of the free surface. An intense sinking process at the frontal surface, with a consequent strong convergence at the front near the sea surface, was observed. He extended this study and developed a hydrodynamical model of upper ocean fronts (Garvine, 1979). Because Garvine's model is quasi-steady, it shows the wind stress playing a secondary role. However, it is well known that this is not actually the case.

wind stress playing a secondary role. However, it is well known that this is not actually the case.

McVean and Woods (1980) considered the formation of a two-dimensional upper oceanic front forced by a barotropic horizontal stretching deformation field, where the long front flow is geostrophic. While assuming a deformation rate of 10^{-5} sec^{-1}, their solutions showed a surface density discontinuity in three to four days. In their study, the frontogenesis in the temperature field depended on the initial inclination of the isotherms to the isopycnics. Furthermore, the isotherm pattern penetrated deeper than the isopycnal pattern.

The disparity in the solutions obtained for the temperature and the density fields are very consistent with observations. Typical examples are the subarctic front and the subtropical front, in the winter season, where a lack of baroclinicity is observed. However, because of the weakness of the temperature gradient in the summer season, a moderate baroclinicity is observed in the subtropical front (Roden, 1974). On the other hand, both the Kuroshio and the Gulf Stream fronts are strongly baroclinic (Roden, 1976).

Kao (1980) studied the dynamics of the establishment and maintenance of the upper oceanic fronts by a western boundary current. The dynamics are controlled by two dimensionless parameters: the thermal Rossby number, Ro, and the Ekman number, E. In his study, while the solutions proved to be similar for a large Ro, the normalized equations depended strongly on E alone. After a quasi-steady state is reached and for E much less than unity, a front is formed. An intense geostrophic jet along the front, a cross-front circulation with surface discharge towards the front, and a return flow at a greater depth were observed. Potential vorticity was conserved in the less dense waters.

In this study a numerical model has been developed to better understand the dynamics of the subarctic front. Instead of following the traditional path of spinning up the ocean model from rest in order to "build up" a front, a geostrophically balanced oceanic front is imposed as an initial condition. The fronts to be simulated will have two different forms. In the first case, the front will be parallel to the latitudinal circles, while in the second instance the front will have an undulatory initial form around 42°N. A set of different atmospheric wind forcing, representing a variety of different atmospheric conditions, is imposed upon these two oceanic fronts. The dynamic response of these two fronts to the different atmospheric forcing is carefully studied.

Because a four-layer numerical model is employed, a better understanding of the dynamical response of the ocean at the wake of a storm is achieved. As a matter of fact, the previous studies that dealt with the cyclone's problem employed a two-layer model. Basically, our results show a close agreement with Geisler's linear solutions (1970). This research confirms that water is upwelled in the first 300 meters at the wake of the cyclone. This upwelling is of the order of 20 meters.

Vertical oscillations, related with inertia gravity waves induced by the storm's passage are observed (Chang and Anthes, 1979). The e-folding time scale of these vertical oscillations is calculated to be of the order of 10 days. This value confirms the fact that in the absence of any external forcing, the induced kinetic energy is quickly redistributed. After a week of the storm's passage, the water remains upwelled in the first 300 meters. It can be concluded that upwelling will continue for several weeks.

A region of relative maximum convergence is observed in the lower layers below a region of relative maximum upwelling in the upper layer, which may be explained by continuity.

Roden demonstrated that frontogenesis is strongly favored when $\partial\tau^x/\partial y$ is strongly positive. Such is the case for the subarctic front which happens to be located to the south of the maximum westerlies, which, in turn, will generate a convergence zone in that region. This particular result has been confirmed during the course of the present research when the classical case of westerlies to the north and easterlies to the south of the front is simulated.

Parallel to the numerical aspect of the present research, some theoretical problems are also addressed. One of these problems is to study the barotropic stability of the subarctic front. It has been proved that if $|\overline{u}-c|^2 \geq g \cdot \overline{h}\ \overline{u}'^2\ \Delta\rho/4f^2\rho_0$ everywhere, the front is stable. Another theoretical result of the present study shows that the time scale of dissipation of horizontal friction is extremely large.

It has been observed that numerical instability is caused when the constancy in the density jump between layers is maintained during the whole time integration. This instability is usually overcome by removing such a constancy (McNider and O'Brien, 1973). A detailed analysis explaining the reason for this numerical instability has been conducted. In decomposing the vertical modes of the linearized model equation, it is shown that the phase speed of the baroclinic modes is larger in the case where the density jump is constant than in the case of the density values arbitrarily chosen.

where the density jump is constant than in the case of the density values arbitrarily chosen.

This research develops a better understanding of frontal oceanic response to atmospheric variations. With a simple numerical model, the principal atmospheric forcings due to the wind action have been simulated. In some cases, these results can be extended easily to other oceanic fronts located in other geographical areas. However, there are still many problems that need to be studied. Thermodynamic processes such as radiative fluxes, precipitation and evaporation need to be implemented in a numerical model of an oceanic front. The numerical simulation of such phenomena will definitively represent a new challenge to the numerical modeller. A different track will have to be followed without the present advantage of using density as a vertical coordinate, as density will no longer be constant either in space or in time. In other words, a hydrothermodynamical model will have to be implemented in such a way that the simple Lagrangian formulation of the numerical model used in this study will no longer be valid.

2. THE MODEL

Consider a stably stratified, hydrostatic, rotating fluid where the Boussinesq approximation is made. The model consists of five incompressible layers which have initial densities ρ_j and thickness h_j, so that $j = 1(1)5$, counting down from the upper layer. The barotropic wave modes are characterized by a very large propagational speed compared with that of the baroclinic wave modes. Because the lowest layer, layer 5, is assumed to be infinitely deep, we can consider it to be at rest everywhere. With this assumption, all the external barotropic modes are filtered out. The free surface of the uppermost layer, δ, remains at a height H above the ground. It is obvious that the relation

$$H = \sum_{i=1}^{5} h_i \tag{1}$$

must hold. The j-th layer has an initial constant thickness, h_j, a constant density ρ_j, and a pressure P_j of the form

$$P_j = P_a + \rho_1 g\delta + g\sum_{i=1}^{j-1} \rho_i h_i + g\rho_j \left[\sum_{i=j}^{5} h_i - z\right] \tag{2}$$

at any point (x, y, z) inside this layer, where P_a is the atmospheric pressure.

Because the lowest layer is considered at rest during the whole time integration, the following relation holds:

$$\nabla\left[\sum_{i=1}^{5} \rho_i h_i + \rho_1 \delta\right] = 0 \tag{3}$$

$$\nabla\left[\sum_{i=1}^{5} \rho_i h_i + \rho_1 \delta\right] = 0 \tag{3}$$

where ∇ represents the horizontal gradient.

Eliminating ∇h_5 and $\nabla\delta$ from (1) and (3) yields

$$\nabla h_1 = -\nabla \sum_{i=2}^{5} h_i \tag{4}$$

$$\nabla\delta = -\nabla \sum_{i=1}^{5} (\rho_i/\rho_1) h_i \tag{5}$$

Neglecting horizontal variations of the atmospheric pressure, P_a, (2) can be rewritten as

$$\nabla P_j = g\nabla[\rho_1\delta + \sum_{i=1}^{j-1} \rho_i h_i + \rho_j \sum_{i=j}^{5} h_i] \tag{6}$$

The substitution of (4) and (5) in this last expression, after some algebraic manipulations, yields

$$\nabla P_j = -g\nabla[\sum_{i=2}^{5} \rho_i h_i - \sum_{i=2}^{j-1} \rho_i h_i - \rho_j \sum_{i=j}^{5} h_i] \tag{7}$$

Therefore, the pressure gradient, ∇P_j, will have an expression of the form

$$\nabla P_j = g\nabla[\sum_{i=j+1}^{5} (\rho_j - \rho_i) h_i] \tag{8}$$

Equation (8) is not very useful as it stands because it contains terms of the lowest layer (which remains motionless during the whole time integration). Therefore, it is advisable to substitute h_5. The following relation holds:

$$\nabla h_5 = -\nabla \sum_{i=1}^{4} h_k \tag{9}$$

The substitution of (8) into (9) yields a final expression for ∇P_j of the form

$$\nabla P_j = g \sum_{i=1}^{4} (\rho_5 - \rho_\nu) \nabla h_i \tag{10}$$

form

$$\nabla P_j = g \sum_{i=1}^{4} (\rho_5 - \rho_\nu) \nabla h_i \tag{10}$$

where $\nu = \max(i, j)$.

Taking into consideration equation (10) the basic horizontal momentum equations for the j-th layer may be expressed as

$$\frac{du_j}{dt} - fv_j = -g \sum_{i=1}^{4} \left[\frac{\rho_s - \rho_v}{\rho_j}\right] \frac{\partial h_i}{\partial x} + A\nabla^2 u_j + \frac{\tau^x}{\rho_1 h_1} \tag{11}$$

$$\frac{dv_j}{dt} + fu_j = -g \sum_{i=1}^{4} \left[\frac{\rho_s - \rho_v}{\rho_j}\right] \frac{\partial h_i}{\partial y} + A\nabla^2 v_j + \frac{\tau^y}{\rho_1 h_1} \tag{12}$$

where $f = f_o + \beta y$ and $\frac{d}{dt} = \frac{\partial}{\partial t} + u_j \frac{\partial}{\partial x} + v_j \frac{\partial}{\partial y}$. It is worthwhile to notice that the wind stress forcing is exerted only on the top layer. The continuity equation for the j-th layer will have the form

$$\frac{\partial h_j}{\partial t} + \frac{\partial}{\partial x}(u_j h_j) + \frac{\partial}{\partial y}(v_j h_j) = 0 \tag{13}$$

A Cartesian coordinate system, x and y, and the corresponding velocity components, u and v, (which are positive eastward and northward, respectively), is used. The vertical coordinate is density.

This class of model tends to be numerically unstable when the interface(s) reaches the sea surface. A closer look at the problem reveals that this numerical instability is most commonly caused by the imposition of closed walls. While working with closed boundaries, the accumulation or removal of water mass at both northern and southern boundaries, caused by the Ekman drift, tends to increase in an unrealistic form. As extreme atmospheric forcing functions are applied in this study, this type of numerical instability appears very quickly. As this is not an acceptable solution to the problem, an alternative is required. On the other hand, from an objective point of view, it is As this is not an acceptable solution to the problem, an alternative is required. On the other hand, from an objective point of view, it is philosophically inconsistent to impose closed walls where they do not exist.

The approach taken here is quite simple. By scaling the x-momentum equation, the two leading terms are selected. These are the Coriolis and the wind stress terms. Now the meridional velocity, v, can be determined at the northern and southern boundaries as a function of the wind stress. As a consequence, the Ekman drift at both boundaries is prescribed instead of closed walls being imposed. This new approach constitutes a clear improvement, as the numerical instability caused by the intersection of the interface with the sea surface at the boundaries is avoided. Furthermore, with the present approach there is no constraint either to terminate the time integration or to switch to a hydrothermodynamical system.

The model geometry is an idealization of the North Pacific Ocean. At both eastern and western boundaries, periodic boundary conditions are implemented. The east-west extension of the basin is approximately 13,000 km, which roughly represents the distance between the two continental areas. Of particular interest is the dynamics of the mid-ocean, in particular in a subregion of 1,000 km along the x-axis. A stretching coordinate is implemented along this axis in such a way that the number of grid points close to the eastern and western boundaries is minimal. At the same time, the distance between grid points is constant in the region of interest.

The same philosophy is applied for the meridional coordinate. Because a better resolution is desired in the middle of the N-S extent of the basin, where the oceanic front is initially centered, a stretching coordinate is employed along the y-axis in a way such that the distance

the basin, where the oceanic front is initially centered, a stretching coordinate is employed along the y-axis in a way such that the distance

between grid points near the front is of the order of 4 kms. Since there is no interest in considering the boundary effects at the northern and southern boundaries, the basin is extended from 30-54°N, while the region of interest lies between 40 and 44°N. Again, the number of grid points away from the region of interest is reduced to a minimum. Therefore, the region of interest consists of a flat-bottomed ocean basin, whose east-west extension is on the order of 1,000 kms, while the north-south extension is on the order of 450 kms.

Because of the particular interest in considering the dynamical response of the subarctic front caused by a cyclone travelling from north to south, a second rectangular basin, following the same idea described above, is implemented. In this case, the inner mesh has an extension of 200 kms and 1,000 kms in the E-W and N-S directions, respectively. On the other hand, the dimensions of the outer mesh in the x- and y-directions are of 1,000 kms and 5,900 kms, respectively.

Two initial formulations of oceanic fronts are considered. In both cases the oceanic fronts, centered in the middle of the north-south extent of the basin, are determined by a hyperbolic tangent of the form

$$h_j = h_{jo} - \Delta h_j \tanh\left(\frac{y^*-W/2}{L_y}\right) \qquad (14)$$

where the subindex j represents the j-th layer so that j = 1(1)5, counting down from the upper layer and W represents the width of the basin. In the first formulation

$$y^* = y, \qquad (15.a)$$

while in the second one

$$y^* = y, \qquad (15.a)$$

while in the second one

$$y^* = y + B \sin kx\ , \qquad (15.b)$$

where B (= $L_y/3$) is the amplitude and k (= $2\pi/\lambda$) is the zonal wavenumber. The value of the wavelength, λ, is arbitrarily chosen to be 500 kilometers, so as to model an initially meandering front. These oceanic fronts are in geostrophic balance with the Coriolis parameters in such a way that

$$u_j = -(g/f) \sum_{i=1}^{4} \left(\frac{\rho_5 - \rho_\nu}{\rho_j}\right) \frac{\partial h_i}{\partial y} \tag{16}$$

By continuity, the meridional velocity, v, in the first case (front without waves) is equal to a constant, which is set to be equal to zero. In the second formulation, because of the undulatory initial form of the oceanic front around 42°N, the meridional velocity is determined by

$$v_j = (g/f) \sum_{i=1}^{4} \left(\frac{\rho_5 - \rho_\nu}{\rho_j}\right) \frac{\partial h_i}{\partial x} \tag{17}$$

It is desirable to study the dynamical response of the temperature and the salinity fronts at the wake of a strong cyclone. For this purpose an initial temperature front is implemented in the model via an hyperbolic tangent of the form:

$$T_j = T_{\bullet j} - \Delta T_j \tanh\left(\frac{y^* - W/2}{L_y}\right) \tag{18}$$

where T_j represents the temperature of the j•th layer (Fig. 1a). An initial salinity front is simulated, via the equation of state, by the relation:

$$S_j = (\rho_j - X_j^0 + aT_j)/b \tag{19}$$

where S_j represents the salinity of the j•th layer, and a and b represents the coefficients of thermal expansion and saline contraction, respectively (Fig. 1b). The constant X_j^0 has the form:

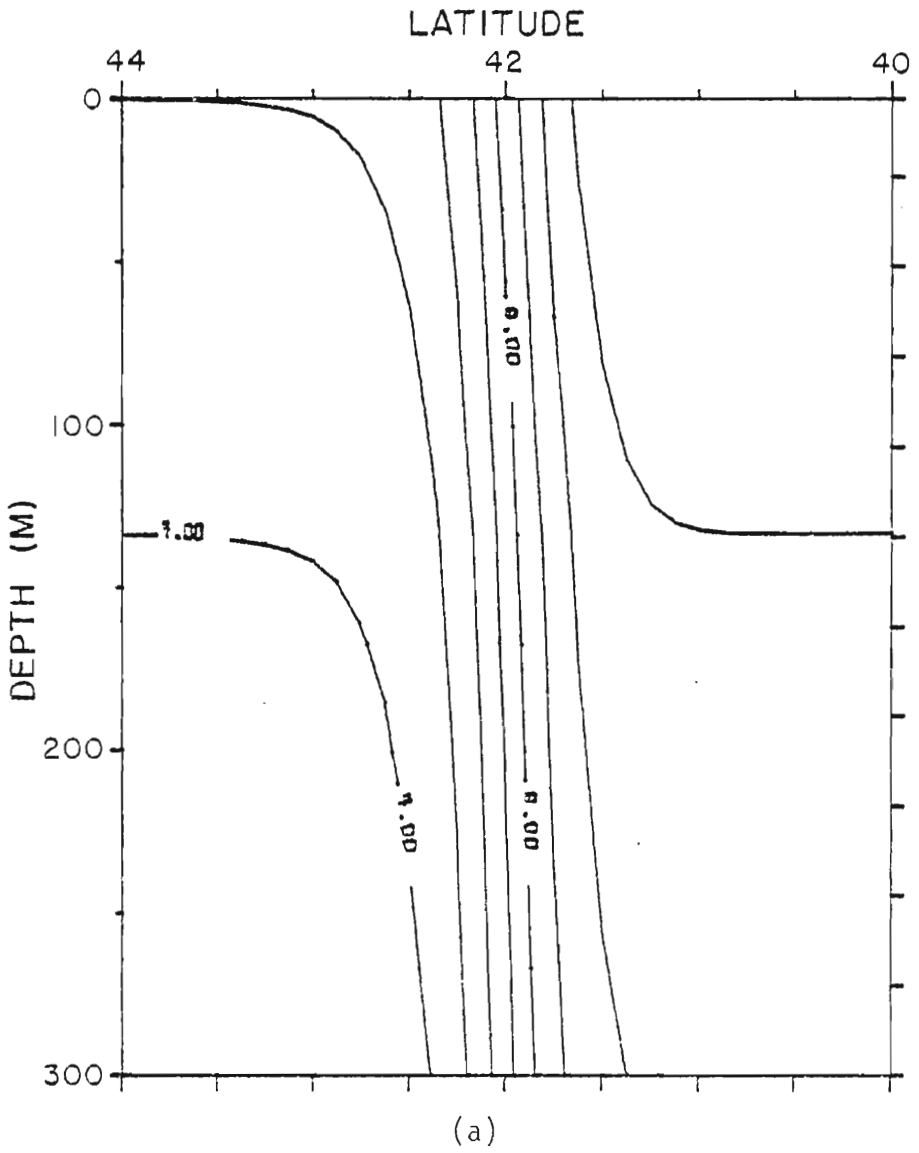

Figure 1. Initial position of the: a) temperature, and b) salinity fronts, in the (y, z) plane.

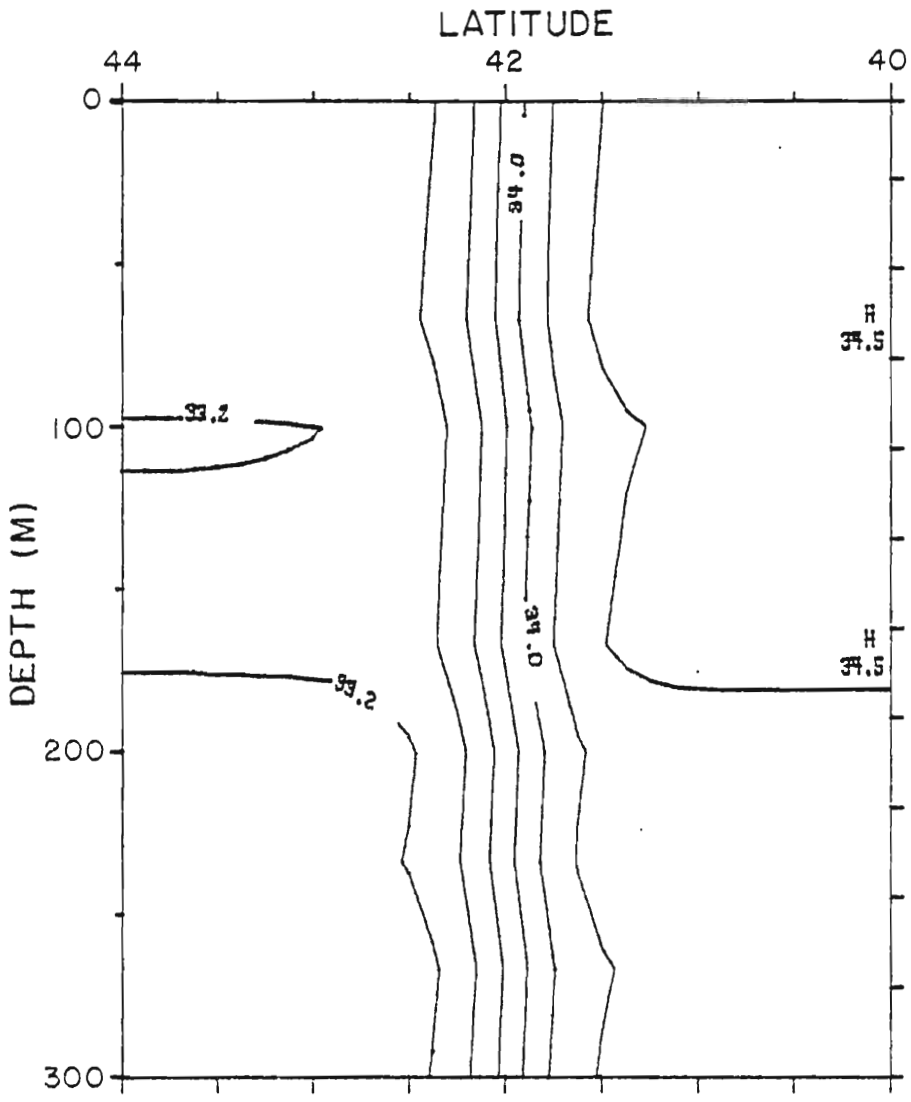

(b)

$$X_j^0 = \rho^0 + aT^0 - bS^0 \qquad (20)$$

where the superscript "0" represents a state of reference. The model representation of the temperature and salinity fronts is in good agreement with Roden's (1976) observations of such fronts.

The temperature is prognostically evaluated, at time step n + 1, by the relation:

$$\frac{dT}{dt} = 0 \qquad (21)$$

while the salinity is diagnostically evaluated by (19).

No flux of temperature or salinity across the boundaries is allowed. Thus, the relation $\frac{\partial T}{\partial n} = \frac{\partial S}{\partial n} = 0$, holds for the four boundaries, where the symbol $\frac{\partial}{\partial n}$ stands for the normal derivative.

The atmospheric forcing used in this research is rather extreme. Although the oceanic fronts are imposed as an initial condition, the severity of the different atmospheric forcing being used may be justified by the fact that this research focuses on the dynamical effects that these different forcings exert on the oceanic front in a very short time scale. A more practical reason is the purpose of saving computer time during the numerous try-outs.

One case study is the dynamical effects caused by the atmospheric westerly winds. For this purpose, a wind stress of 10 dynes cm^{-2} blows toward the eastern boundary at all grid points during the whole time integration. Another case study is the effect of the passage of a severe atmospheric front. Initially located at 1,000 km to the west of our region of interest, the atmospheric front travels across the basin at a

speed of 500 kms/day from the NW to the SE corner. Behind the atmospheric front, the northwesterly winds are represented by the formulation

$$\tau^y = -T_o \sin\theta \qquad (22.a)$$

$$\tau^x = T_o \cos\theta \qquad (22.b)$$

where the amplitude of the wind stress, T_o, and the angle that the atmospheric front forms with the x axis, θ, are given arbitrary values of 7 dynes/cm^2 and 45°, respectively.

The effects caused by the passage of a strong atmospheric cyclone are considered. A westerly wind stress of 2 dynes/cm^2, initially imposed, is suddenly interrupted by the passage of this cyclone traveling towards the eastern boundary at a speed of 500 km/day. The circumferential velocity of this cyclone, υ, is formulated in the following manner:

$$\upsilon = |\underset{\sim}{V}| = \begin{cases} v_o(1+r/r_o)^{-1} & 10 \leq r \leq 500 \text{ kms} \\ 0 & r \leq 10 \text{ kms} \end{cases} \qquad (23)$$

where $r^2 = r_x^2 + r_y^2$, and v_o is equal to 70 m. s^{-1}.

Having determined υ, the wind stress of the cyclone may be computed as follows

$$\tau^x = \rho_a c_D |\underset{\sim}{V}| u \qquad (24.a)$$

$$\tau^y = \rho_a c_D |\underset{\sim}{V}| v \qquad (24.b)$$

Typical values of ρ_a (= 10^{-3} g cm^{-3}), c_D (= $2.5.10^{-3}$) and r_o (= 75 km) are used.

The classical effect of westerlies at the north and easterlies at (= 75 km) are used.

The classical effect of westerlies at the north and easterlies at the south of the oceanic front is also addressed. The curl is

represented by a cosine function

$$\tau^x = -T_1 \cos(\pi y*/W) \tag{25}$$

where T_1 is given the value of 10 dynes cm^{-2}. The value of τ^y is set to be equal to zero.

For the purpose of saving computer time and in order to avoid the numerical noise produced by the higher wave number, the model equations are integrated in a staggered grid in space. The staggering of the grid is such that the zonal velocity points, u, alternate with height points, h, along the latitudinal direction, while the meridional velocity points, v, alternate with height points, h, along the meridional direction.

The nonlinear terms are expressed in the "semimomentum" formulation. This scheme is used to ensure the elimination of fictitious sources of kinetic energy.

The model consists of four active layers of depth

$$h_1 = 3K,\ h_4 = h_3 = h_2 = K,\ K = 50\ m. \tag{26}$$

The first layer is chosen to be that deep because it has been observed that both the salinity and temperature fronts tend to compensate in the first 150 meters.

The vertical density profile is constructed so that there is a difference of 2.10^{-3} g cm^{-3} between the first and second layers, a difference of 3.10^{-4} g cm^{-3} between the two bottom layers, and differences of 5.10^{-4} g cm^{-3} between the remaining layers.

3. ON THE ROLE OF HORIZONTAL FRICTION

An attempt to determine the time scale of dissipation of an oceanic front is made. The study is conducted in such a way that if the time scale of the dissipation of the oceanic front is larger than the time scale of the perturbation produced by the wind stress, it is possible to neglect lateral friction. Because the longitudinal frontal length scale, L_y, is smaller than the latitudinal frontal length scale, L_x, the derivatives with respect to x will be neglected as compared to the derivatives with respect to y. A simple, two-layer model is considered. The lower layer, layer 2, is chosen to be infinitely deep in such a way that the barotropic mode is filtered out. The trivial solution $u_2 = v_2 = 0$ follows quite naturally.

The pressure in the upper layer, layer 1, will have the form

$$P_1 = P_a + \rho_1 g(h_1 - z) + \rho_2 g(H - h_1) \tag{27}$$

where P_a represents the atmospheric pressure and z is measured from the bottom. The gradient of P_1 yields

$$\nabla P_1 = -\rho_1 \, g^* \nabla h_1 \tag{28}$$

where $g^* = g\left(\frac{\rho_1 - \rho_2}{\rho_1}\right)$ represents the reduced gravity. The horizontal fluctuations of the atmospheric pressure are neglected in the present study of friction. For convenience, the subindex 1, representing the

study of friction. For convenience, the subindex 1, representing the

upper layer, will be omitted. The equations of motion for the upper layer are

$$\frac{\partial u}{\partial t} + v\frac{\partial u}{\partial y} - fv = A\frac{\partial^2 u}{\partial y^2} \tag{29}$$

$$\frac{\partial v}{\partial t} + v\frac{\partial v}{\partial y} + fu = -g^*\frac{\partial h}{\partial y} + A\frac{\partial^2 v}{\partial y^2} \tag{30}$$

$$\frac{\partial h}{\partial t} + \frac{\partial}{\partial y}(vh) = 0 \tag{31}$$

where the forcing due to the wind stress terms is neglected in order to retain only the forcing due to the frictional terms.

This non-linear set of equations is not easy to solve. It is assumed that the frictional effect will slowly change a steady, inviscid initial front, and a perturbation solution is sought by assuming that friction has a weak effect.

For this steady oceanic front to persist, the interface, h_o, must be balanced initially by a zonal velocity of the form

$$u_o = -\left(\frac{g^*}{f}\right)\frac{\partial h_o}{\partial y} \tag{32}$$

where the subscript "o" stands for the basic state.

The interface has a mean value, h_{oo}, while its variation is chosen to have a hyperbolic tangent centered in the middle of the N•S extent of the basin. Therefore, the initial thickness of the upper layer is represented as

$$h_o = h_{oo} - \Delta h \tanh\left(\frac{y-W/2}{L_y}\right) \tag{33}$$

$$h_o = h_{oo} - \Delta h \tanh\left(\frac{y-W/2}{L_y}\right) \tag{33}$$

where Δh represents the maximum amplitude of the interface perturbation.

By continuity, the meridional velocity, v, is initially set to be zero.

The viscous perturbation solutions are obtained by assuming the value of A to be very small. Let

$$u = u_o + u' \tag{34a}$$

$$v = v_o + v' \tag{34b}$$

$$h = ho + h' \tag{34c}$$

where the perturbation variables (which are of order A) are denoted by primes. The equations for the upper layer then become

$$\frac{\partial u'}{\partial t} - v'\left(\frac{g^*}{f}\right)\frac{\partial^2 h_o}{\partial y^2} + v'\frac{\partial u'}{\partial y} - fv' = -\left(\frac{Ag^*}{f}\right)\frac{\partial^3 h_o}{\partial y^3} + A\frac{\partial^2 u'}{\partial y^2} \tag{35}$$

$$\frac{\partial v'}{\partial t} + v'\frac{\partial v'}{\partial y} + fu_o + fu' = -g^*\frac{\partial h_o}{\partial y} - g^*\frac{\partial h'}{\partial y} + \frac{\partial^2 v'}{\partial y^2} \tag{36}$$

$$\frac{\partial h'}{\partial t} + \frac{\partial}{\partial y}(h_o v') + \frac{\partial}{\partial y}(v'h') = 0 \tag{37}$$

The terms $v'\frac{\partial u'}{\partial y}$, $v'\frac{\partial v'}{\partial y}$, $\partial(v'h')/\partial y$, $A\frac{\partial^2 u'}{\partial y^2}$, and $A\partial^2 v'/\partial y^2$ are of second order. Thus, they are negligible. The terms fu_o and $-g^*\partial h_o/\partial y$ represent the basic state balance. In order to filter out the gravity waves, the term $\partial v'/\partial t$ is omitted. With these simplifications, the above equations reduce to linear perturbation equations of the form

$$\frac{\partial u'}{\partial t} - \left(\frac{g^* v'}{f}\right)\left(\frac{\partial^2 h_o}{\partial y^2} + f^2/g^*\right) = -\left(\frac{Ag^*}{f}\right)\frac{\partial^3 h_o}{\partial y^3} \tag{38}$$

$$u' = -(g^*/f)\frac{\partial h'}{\partial y} \tag{39}$$

$$\frac{\partial h'}{\partial t} + \frac{\partial}{\partial y}(v'h_o) = 0 \tag{40}$$

To solve this system, a single equation for v' is first needed. Replacing the value of u' in (38) yields

$$-\frac{g^*}{f}\frac{\partial^2 h}{\partial y \partial t} - \frac{g^*}{f} v'\left(\frac{\partial^2 h_o}{\partial y^2} + f^2/g^*\right) = -\left(\frac{Ag^*}{f}\right)\frac{\partial^3 h_o}{\partial y^3} \tag{41}$$

Applying the operator $(g^*/f)\frac{\partial}{\partial y}$ to (40), it follows that

$$\left(\frac{g^*}{f}\right)\left(\frac{\partial^2 h'}{\partial t \partial y} + \frac{\partial^2}{\partial y^2}(v'h_o)\right) = 0 \tag{42}$$

The addition of (41) and (42) yields

$$\frac{\partial^2 V}{\partial y^2} - \left(\frac{\partial^2 h_o/\partial y^2 + f^2/g^*}{h_o}\right)V = -A\frac{\partial^3 h_o}{\partial y^3} \tag{43}$$

where V $(= v'h_o)$ is the mass transport in the upper layer. The boundary conditions are such that the meridional mass transport, V, is set to be zero at both the northern an southern boundaries. It is of interest to note that v is independent of time.

As $h_o(y)$ is a known function, the coefficients of (43) are known and this equation can be rewritten as

$$\frac{\partial^2 V}{\partial y^2} - F(y)V = -G(y) \tag{44}$$

where

$$F(y) = \frac{\frac{\partial^2 h_o}{\partial y^2} + f^2/g^*}{h_o} \tag{45a}$$

and

$$G(y) = A\frac{\partial^3 h_o}{\partial y^3} \tag{45b}$$

In order to cover a wider range of oceanic fronts, two different

In order to cover a wider range of oceanic fronts, two different

meridional length scales, L_y, are considered. The chosen dimensions are 1 and 50 kilometers, respectively. In the first case, an approximate

value of F(y) is:

$$F(y) \doteq \frac{f^2/g^*}{h_o} \tag{46}$$

while in the second case, F(y) has an approximate value of:

$$F(y) \doteq \frac{\partial^2 h_o/\partial y^2}{h_o} \tag{47}$$

Using the first approximation, (44) may be rewritten as:

$$\frac{\partial^2 V}{\partial y^2} - \alpha^2 V = -A\frac{\partial^3 h_o}{\partial y^3} \tag{48}$$

where $\alpha^2 = f^2(g^*h_o)^{-1}$ is the inverse of the Rossby radius of deformation squared. For this particular case, an analytical solution can be obtained. If the Ekman number is set to be equal to 0.1, the resulting value of A is then 10 $m^2 sec^{-1}$. The scaling of (48) shows that the first and third terms are the largest ones, by two orders of magnitude. Therefore, (48) has the form

$$\frac{\partial^2 V}{\partial y^2} = -\frac{2A\Delta h}{L_y}\left(\frac{2\sinh^2\left(\frac{y-W/2}{L_y}\right) - 1}{\cosh^4\left(\frac{y-W/2}{L_y}\right)}\right) \tag{49}$$

The analytical solution of this expression is

$$V(y) = \frac{-A\Delta h}{L_y}\,\mathrm{sech}^2\left(\frac{y-W/2}{L_y}\right) \tag{50}$$

The integration, with respect to time, of the continuity equation yields a perturbation expression for the interface, h', of the form

yields a perturbation expression for the interface, h', of the form

$$h' = \frac{\partial V}{\partial y}\,t \tag{51}$$

Considering the worst possible situation, the smallest time scale of dissipation, T, is defined in such a way that

$$T = h' \left| \frac{\partial V}{\partial y} \right|_M^{-1} \tag{52}$$

where $\left| \frac{\partial}{\partial y} \right|_M$ represents the maximum absolute value of such derivative. The value of h' is arbitrarily set up to be equal to 10 meters. For different values of A and L, different values of $\left| \frac{\partial V}{\partial y} \right|_M$ may be obtained. A list summarizing these cases is condensed in table 1.

However, this solution is restricted to oceanic fronts of the order of one kilometer. As it is stated previously, the subarctic front has a meridional length scale of the order of thirty kilometers. A new scaling of (48) using this length scale, reveals that the three terms of this equation are comparable. Thus, the full equation has to be solved.

In using a meridional length scale of 50 kilometers, (48) has the form:

$$\frac{\partial^2 V}{\partial y^2} - \frac{\partial^2 h_o}{\partial y^2} \frac{V}{h_o} = -A \frac{\partial^3 h_o}{\partial y^3} \tag{53}$$

The general solution of the corresponding homogeneous equation (53), $V_c(y)$, is:

$$V_c(y) = C_1 V_1 + C_2 V_2 \tag{54}$$

where $V_1 = h_o$, $V_2 = h_o \int h_o^{-2} dy$ and C_1 and C_2 are arbitrary constants. The method of variation of parameters is used to solve the nonhomogeneous equation (48). This method requires the replacement of the constants C_1 and C_2 by two arbitrary functions, $\chi(y)$ and $\zeta(y)$. These arbitrary

equation (48). This method requires the replacement of the constants C_1 and C_2 by two arbitrary functions, $\chi(y)$ and $\zeta(y)$. These arbitrary

functions will be determined in such a way that the particular solution,

$V_p(y)$, has the form

$$V_p(y) = \chi(y)V_1(y) + \zeta(y) \quad V_2(y) \tag{55}$$

The arbitrary function, χ and ζ, must satisfy certain conditions in order to satisfy the nonhomogeneous O.D.E. These conditions are

$$\chi_y V_1 + \zeta_y V_2 = 0$$

$$\chi_y V_{1y} + \zeta_y V_{2y} = \Psi(y) \tag{56}$$

where χ_y, ζ_y, V_{1y} and V_{2y} represent the meridional derivatives of the functions χ, ζ, V_1 and V_2 respectively, and $\Psi(y)$ represents the forcing function defined by

$$\Psi(y) = \left(\frac{2\Delta hA}{L_y^3}\right)\left[\frac{2\sinh^2\left(\frac{y-W/2}{L_y}\right) - 1}{\cosh^4\left(\frac{y-W/2}{L_y}\right)}\right] \tag{57}$$

The system of equation (56) gives us a solution for the functions χ_y and ζ_y. These values are:

$$\chi_y = -V_2(y)\ \Psi(y)/W(V_1, V_2) \tag{58a}$$

$$\zeta_y = V_1(y)\ \Psi(y)/W(V_1, V_2) \tag{58b}$$

where the wronskian, $W(V_1, V_2)$, is equal to one.

The values of χ and ζ, at each grid point, are determined by numerical integration. To achieve this purpose, Simpson's rule is used. Knowing the values of χ and ζ, a final expression for the meridional mass transport, V, can be numerically evaluated at each grid point. Such an expression has the form

$$V(y) = (C_1 + \chi)\ V_1(y) + (C_2 + \zeta)\ V_2(y) \tag{59}$$

Again, by plotting the function $\frac{dV(y)}{dy}$ versus y, a maximum absolute value

Again, by plotting the function $\frac{dV(y)}{dy}$ versus y, a maximum absolute value

of the former function may be determined for different values of A and L_y. Table 2 summarizes these results.

The analysis of Tables 1 and 2 shows the same salient features: a) The larger the coefficient of diffusion, A, keeping L_y constant, the smaller the time scale of dissipation, T; b) The larger the meridional length scale of the oceanic front, L_y, keeping A constant, the larger the time scale of dissipation.

From observations, it is well known that the meridional length scale of the subarctic front is of the order of thirty kilometers. Thus, the results presented in Table 2 take full account of the different alternatives that might occur. These results reflect the same basic conclusion: friction plays no significant role, as the time scale of dissipation due to horizontal friction is very large.

$A(m^2\ sec^{-1})$	$L_y(km)$	$\lvert\frac{\partial V}{\partial y}\rvert_M(m\ sec^{-1})$	$T(sec)$
10	2	2.10^{-5}	5.10^5
10	1	8.10^{-5}	$1.25.10^5$
1	2	2.10^{-6}	5.10^6
1	1	8.10^{-6}	$1.25.10^6$

Table 1. Time scale of dissipation, T, for different values of A, L_y, $\lvert\frac{\partial V}{\partial y}\rvert_M$, using equation (48).

1	10	5.10^{-9}	10^9
1	50	7.10^{-11}	10^{11}
10	10	5.10^{-8}	10^8
10	50	7.10^{-10}	10^{10}
100	10	5.10^{-7}	10^7
100	50	7.10^{-9}	10^9

Table 2. Same as Table 1, but using equation (53).

4. ANALYSIS OF THE NUMERICAL EXPERIMENTS

There is a considerable lack of numerical simulations in the modelling of the mid-oceanic fronts. Even though the observational and theoretical studies performed by Roden are useful because they give us a fairly good idea of the dynamics of the oceanic fronts in the North Pacific Ocean, the supporting numerical modelling of such fronts is lacking.

The aim of this research is to fill, in part, such a vacuum. The emphasis of this study is to understand the role the atmospheric forcing plays on the dynamical structure of the subarctic front. A complete series of different atmospheric wind forcings, which account for all possible atmospheric situations, is designed in order to achieve such a goal.

The approach used here is similar to the one taken by Eliassen and Raustein (1970), the difference being that, while studying the atmospheric front, they chose potential temperature as a vertical coordinate.

In this research, two fronts are simulated. Both of them have a different initial configuration. The philosophy behind the second choice is that the meandering of oceanic fronts is not an infrequent phenomenon (Fig. 2).

The effects of the atmospheric wind forcing have a time scale of a week or two (Roden, 1977). It should be no surprise that we carry out

The effects of the atmospheric wind forcing have a time scale of a week or two (Roden, 1977). It should be no surprise that we carry out our time integration in such a time scale.

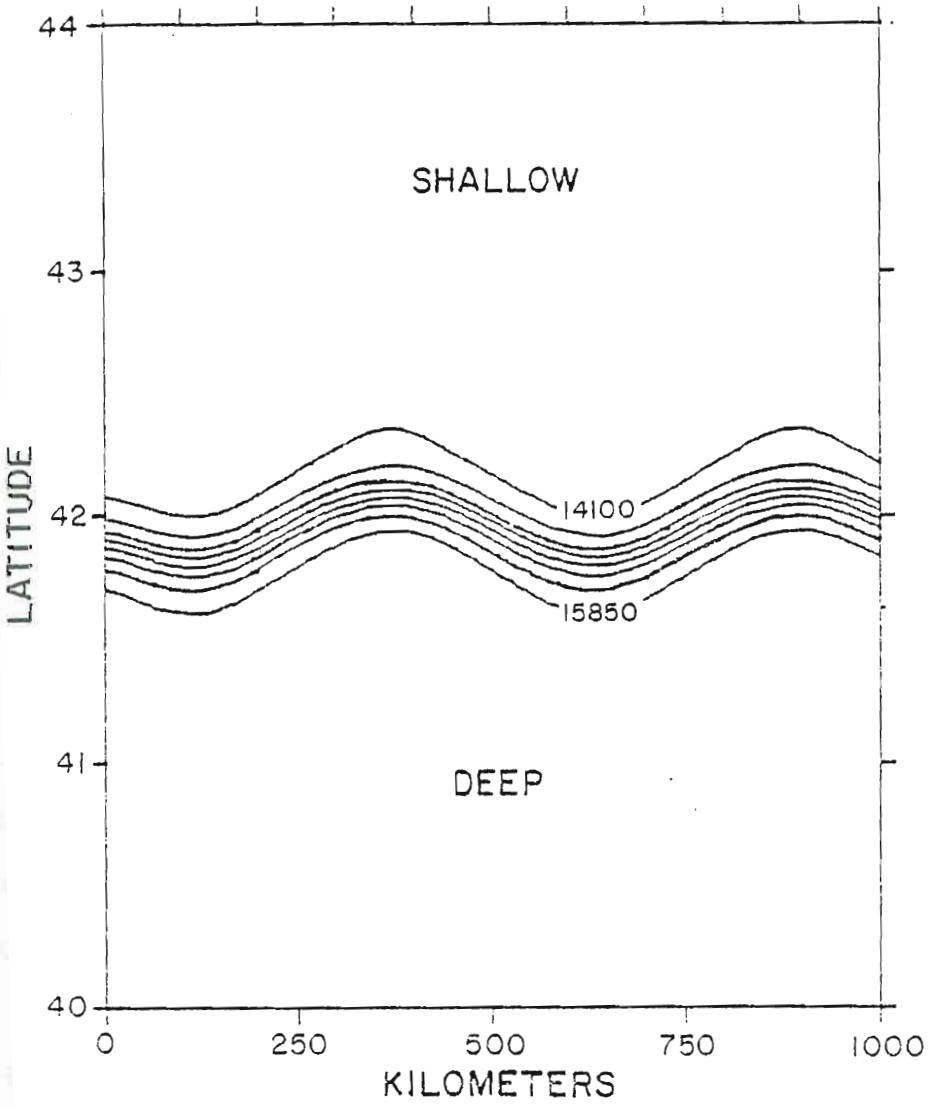

Figure 2. Initial configuration of the height field of the subarctic front when $y_* = y + B\sin kx$ for the first layer in the (x, y) plane. The values in the figures are expressed in the c.g.s. system.

the c.g.s. system.

Two main reasons determine our choice of 150 meters for the depth of the first layer. On one hand it is observed that within that layer both the temperature and the salinity fronts do compensate each other. A very weak density front is thus observed. On the other hand, a high stability layer, which may be used as an index of the depth of the upper layer, is found to be between 100 and 150 meters. The atmospheric forcing is limited to the layer between the sea surface and the high stability layer (Roden, 1970). By contrast in the layer between 150 and 300 meters the density front is pronounced, as the temperature and salinity fronts do not happen to compensate each other. Our experiments tend to confirm the fact that, in the case of the subarctic front, the response to the atmospheric wind forcing is confined to the first 150 meters. The simulation of a strong cyclone constitutes the only exception.

It is widely known that the subarctic front intensifies or decays in response to atmospheric forcings (Roden, 1976). Four different types of atmospheric forcings can be identified: momentum, radiative heat fluxes, precipitation and evaporation, and turbulent energy fluxes. Because frontogenesis in the Central Pacific is largely dependent upon the configuration of the wind stress field, this research focuses on this particular type of atmospheric forcing.

As our study focuses on the dynamics of the mid ocean, the lateral boundary effects are not our concern. The task, therefore, is to set up a model in such a way that the computational boundary effects should not affect nor contaminate the interior solution. To achieve this thrust,
a model in such a way that the computational boundary effects should not affect nor contaminate the interior solution. To achieve this thrust, the model is constructed so that the boundaries are placed far apart

from the region of interest. While pursuing this goal, we try to minimize the number of grid points outside the region of interest by using stretching coordinates. Our first analysis is over an area of 1000 kms in the east-west direction and 450 kms in the north-south direction.

The approach taken here is that a geostrophically balanced oceanic front is imposed as an initial condition, instead of the traditional way of spinning up the ocean model from rest in order to "build up" an oceanic front. Our approach is more efficient and more suitable for the purpose of this research as the ocean model can be run for a short time scale. Obviously, a great amount of computer time is saved using this type of initialization.

All the numerical simulations dealing with the ocean's response to the passage of a strong cyclone had been performed using two layer models. A deeper understanding of the physics of the ocean's response will be gained with the implementation of multilayer models. This is the main reason why a four-layer model is implemented in this study. For a clearer visualization of the physics involved, the pictures (of the u, v and h field solutions) presented hereafter will reproduce the isoanomal field only. That is to say, the departure from the initial state will be plotted.

The first case to be considered is the most frequent one. A uniform westerly wind is imposed at all grid points during the whole period of integration, 10 days. This particular time scale is sufficiently large to give a good idea of the resulting dynamics of the oceanic front in response to this wind. The Ekman flow to the right of the westerlies causes a southward displacement of the subarctic front (Fig. 3). At the

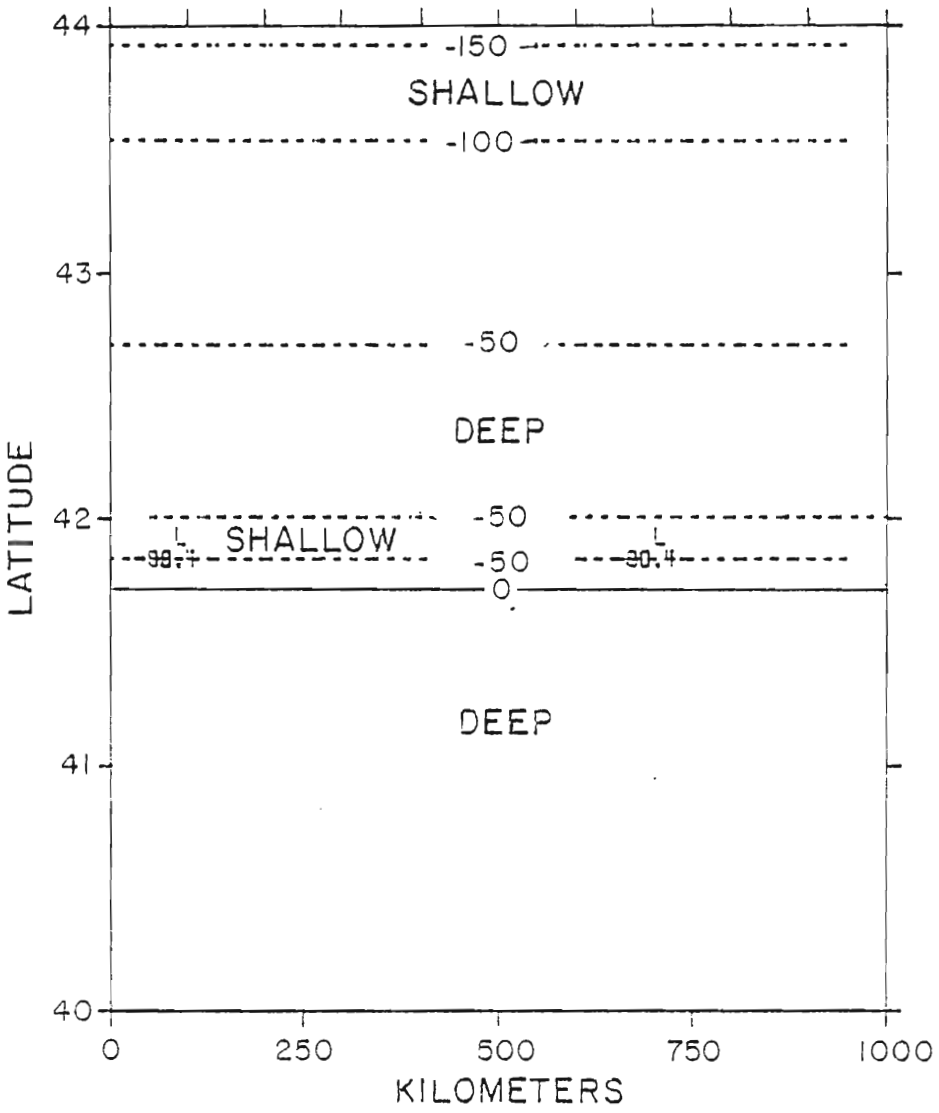

Figure 3. Isoanomalies of the height field for the westerly wind case, after 10 days. The values in the figures are expressed in the c.g.s. system.

case, after 10 days. The values in the figures are expressed in the c.g.s. system.

same time a region of upwelling is detected at the site of the front. This upwelling of water may be explained by the southward Ekman flow. While the geostrophic zonal velocity field, u, shows no change at all, the meridional velocity field, v, shows a southward component, which accounts for the southward Ekman transport and subsequent downwelling at that boundary. No meanders are observed along the front. The stability of the front is thus verified.

It is observed that frontogenesis is stronger where the curl of the wind stress is strongly negative. This feature is observed, in the case of subarctic frontogenesis, on the southern side of the westerly jet. A convergence zone is originated as a consequence of this phenomenon.

The classical case of westerlies at the north and easterlies at the south of the front is also considered. Convergence all over the basin can be detected. The downwelling observed supports the observations of Roden (1977) as the convergence observed favors the frontogenetical effects (Fig. 4).

The response of a horizontally homogeneous ocean to the passage of a strong cyclone has been studied from the observational, theoretical and numerical points of view. Perhaps the most important observational research in this context was performed by Leipper (1967). His observations of the hurricane Hilda of 1964 in the Gulf of Mexico showed the evidence of water having been upwelled from a depth of 60 m. This kind of upwelling explained the drop of 5°C in the sea surface temperature that Leipper recorded in the lee of hurricane Hilda. The numerical simulation of O'Brien and Reid (1967), tends to support this evidence. Implementing a two layer nonlinear model, these authors

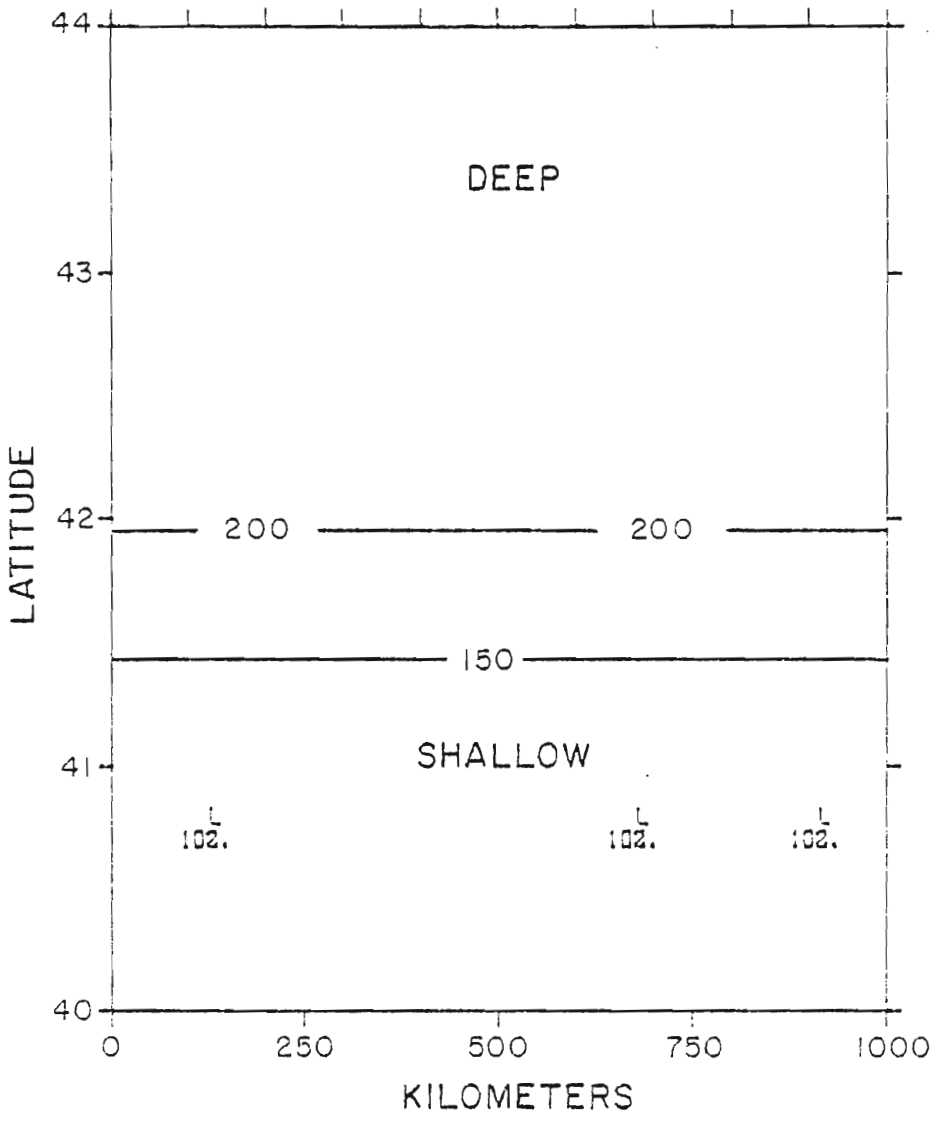

Figure 4. Isoanomalies of the height field of the top layer for the curl case after 10 days.

studied the ocean's response to a stationary, axisymmetric hurricane. They were able to detect a maximum upwelling of 80 meters at 30 kilometers of the center of the hurricane. The fact that upwelling is responsible for the lowering of the sea surface temperature is in sharp contradiction with the basic assumption of Jordan (1964). He estimated that mixing processes, such as precipitation, evaporation and sensible and turbulent heat transfer were responsible for such a phenomenon.

The observational study of Black and Withee (1976) showed the evidence of inertia-gravity waves in the wake of hurricane Eloise of 1975. Because O'Brien and Reid's (1967) hurricane model is stationary, it could not account for these storm induced inertia-gravity waves. In a theoretical study, Geisler (1970) studied the linear response of a two-layer ocean model to a moving hurricane. Whenever the translation speed of the cyclone exceeded the baroclinic long-wave speed, he was able to detect an internal wake in the lee side of the storm.

Chang and Anthes (1978) employed a numerical model to study the ocean's response to a moving hurricane. They showed that vertical motions associated with the inertia-gravity waves persist at the wake of the cyclone's path. Although their numerical model was basically non-linear, their results agree with Geisler's linear solutions.

The next experiment to be simulated is the passage of a strong cyclone moving from west to east, at a speed, S, of 500 kilometers per day, along the centerline of the front. Initially located at 2500 km to the west of our region of interest, the center of the cyclone reaches the western boundary at the end of the fifth day. At the end of the sixth day, the center of the cyclone is located in the middle of the zone of

interest. Figures 5a and b show a shift to the south of the maximum current, as observed by Chang and Anthes (1978).

The center of the cyclone at the end of the seventh day is located at the eastern boundary of our region of interest. Figure 5c shows that the region of maximum uplifting lags the center of the storm by 150 kilometers and is slightly to the right of the center of the cyclone's path. A second maximum uplifting is located about 500 kilometers behind the storm. This second maximum is clearly associated with inertia-gravity waves at the wake of the cyclone. The wave that is observed in the lee of the storm has a wavelength of approximately 350 kilometers. This value is very close to the one observed by Black (1977), 450 kilometers, along the wake of hurricane Ginger of 1971, and the one obtained by Chang and Anthes(1979), of 450 kilometers. The main differences between our model and Geisler's is that our model is nonlinear and that the translation of the cyclone is slower in our simulation. These two factors may account for the slight discrepancy in the obtained values of the wavelength.

According to Geisler's theory, a decay in the direction perpendicular to the storm track, with an e-folding distance equal to the radius of deformation should be expected. In our case, the value of the radius of deformation is less than 20 kilometers. On one hand, this explains the narrowness of the wake behind the storm. On the other hand, as the length scale of the cyclone is greater than the length scale of the baroclinic radius of deformation, small-scale dispersive wave modes are not excited. Therefore, a small amount of energy is dispersed

the baroclinic radius of deformation, small-scale dispersive wave modes are not excited. Therefore, a small amount of energy is dispersed

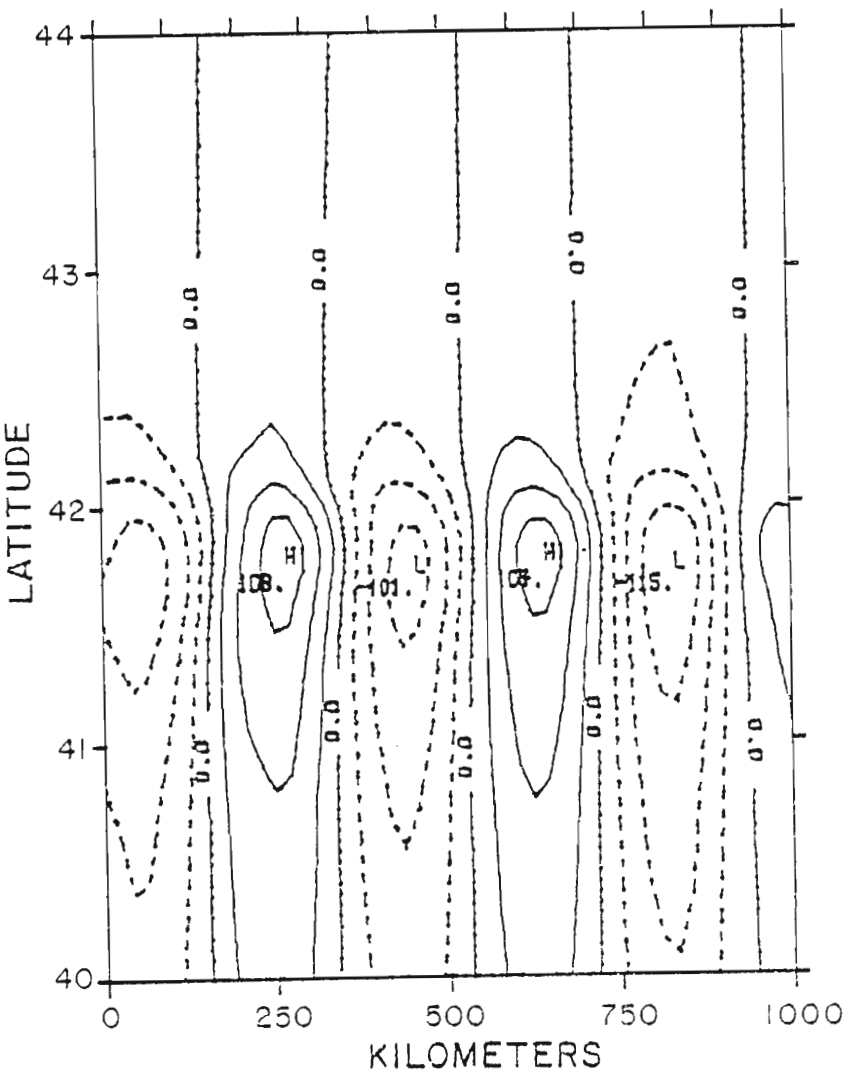

(a)

Figure 5. a) Isoanomalies of the zonal velocity field, u; b) the meridional field, v; c) the height field of the top layer for the cyclone travelling from west to east, after 7 days.

a) Isoanomalies of the zonal velocity field, u; b) the meridional field, v; c) the height field of the top layer for the cyclone travelling from west to east, after 7 days.

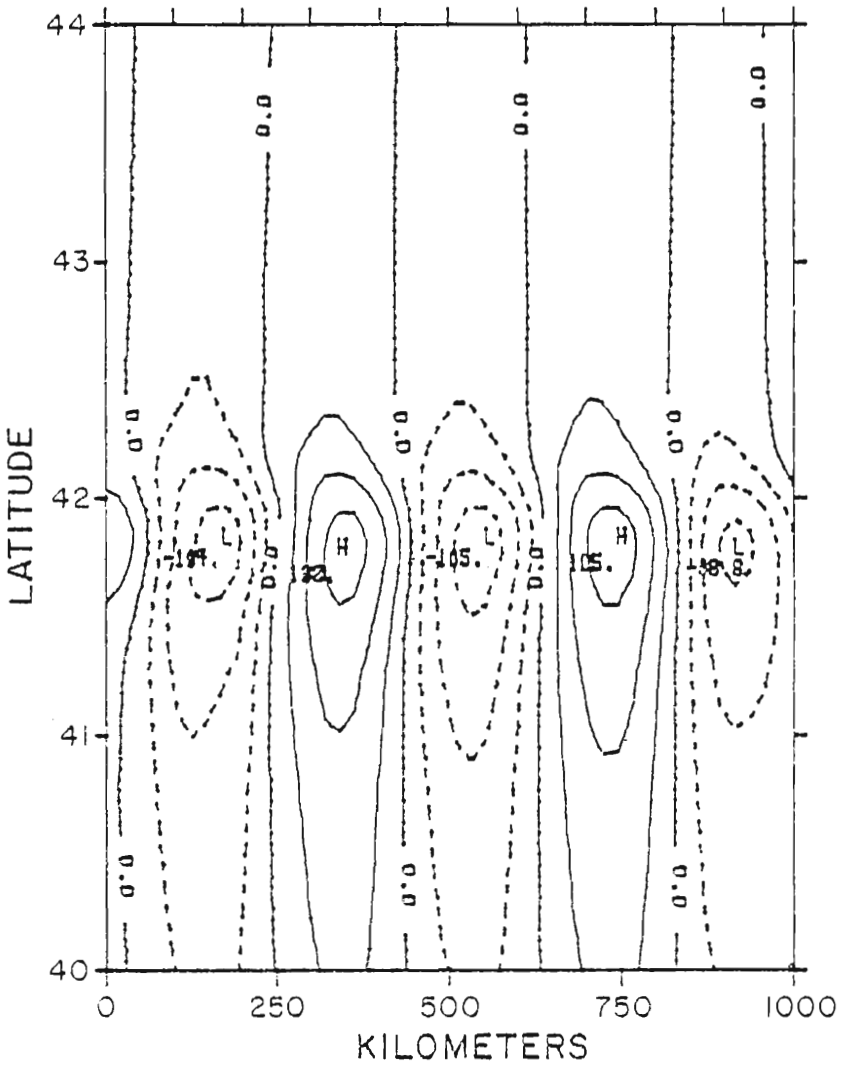

(b)

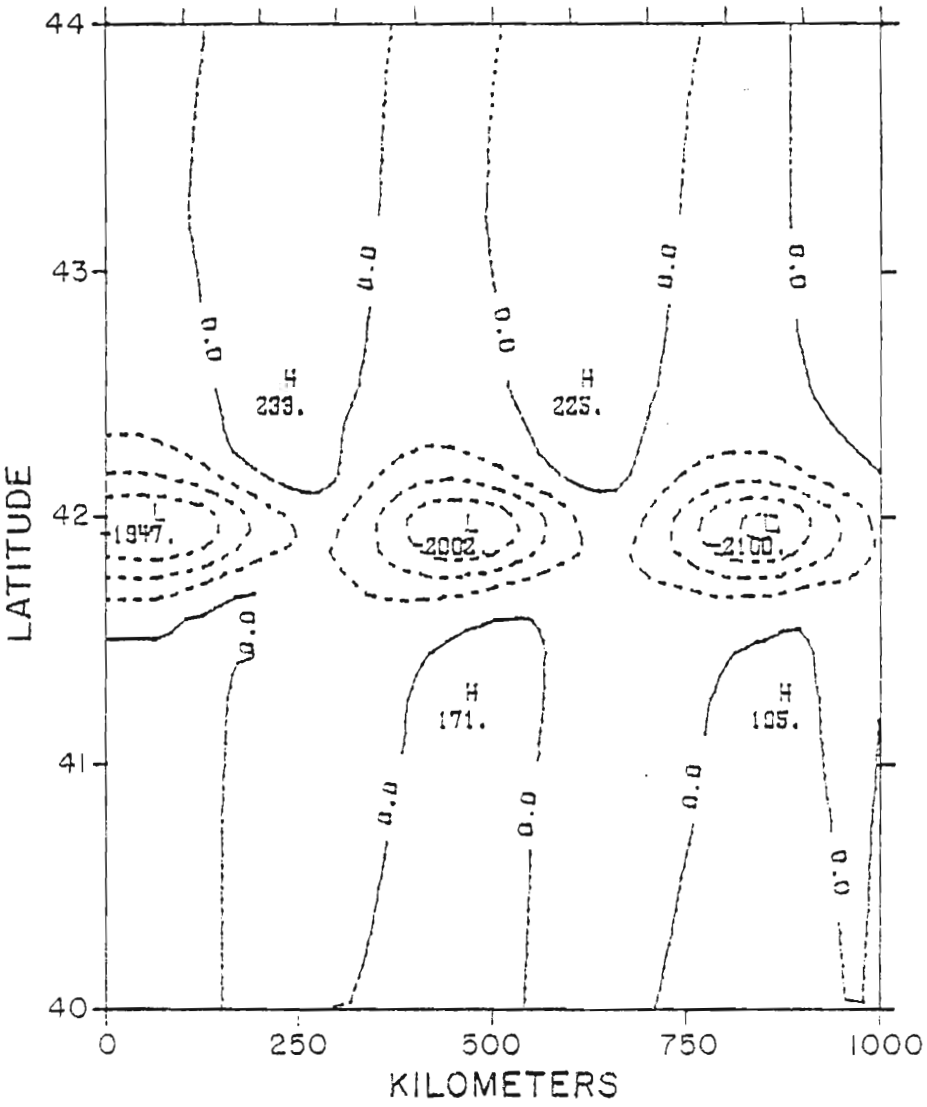
44
43
42
41
40
LATITUDE
0
250
500
750
1000
KILOMETERS
H
233.
H
225.
L
1947.
L
2002.
L
2100.
H
171.
H
125.
0.0

(c)

towards the northern and southern boundaries. Figures 5a, b and c confirm these results.

Permanent baroclinic ridges are observed between upwelled regions (Fig. 5c). Geisler's linear theory establishes that the amplitude of these ridges depends on the vorticity input of the cyclone and not on the rate of input. The particular curvature of the ridges may be explained by the southward trajectory of the water parcels that we have previously discussed.

The counterclockwise motion of the cyclone generates a divergent Ekman flow towards the southern and northern boundaries. Therefore, a belt of "high water mass" is generated, by continuity, at both sides of the front (Fig. 5c). The water displaced away from the front is replaced by a deeper and cooler water mass, thus generating an upwelling effect.

From Fig. 5c it can be seen that the vertical amplitude of the upwelling is of the order of 10 meters. Let us define ΔH to be such an amplitude (Fig. 6):

$$\Delta H(t) = h_1(t) - h_1(o) \tag{60}$$

As we are dealing with an incompressible fluid, the vertically integrated continuity equation for the top layer is:

$$-\frac{1}{h_1}\frac{\partial}{\partial t}(\Delta H) = \left(\frac{\partial u}{\partial x} + \frac{\partial v}{\partial y}\right) \tag{61}$$

where $-\frac{\partial}{\partial t}(\Delta H)$ represents the velocity of upwelling.

By simple scaling, it is inferred that

By simple scaling, it is inferred that

$$-fv = -g^* \frac{\partial h}{\partial x} + \tau^x/\rho_o h_1 \tag{62}$$

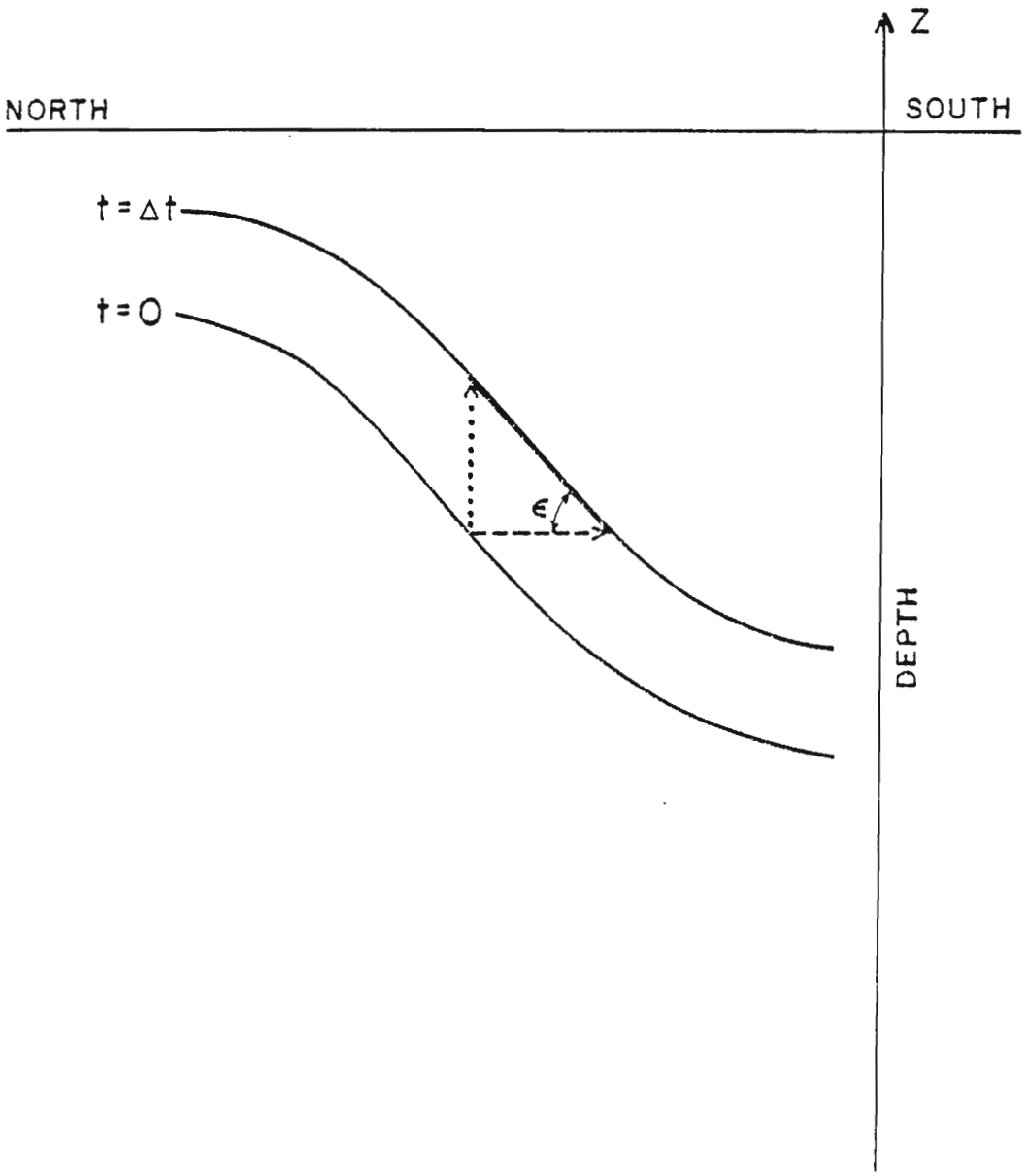

Figure 6. Relative positions of the first interface, represented by a solid line, near the front in the (y, z) plane at times $t = \Delta t$ and $t = 0$. The dotted line represents the vertical motion of the first interface, while the dashed line represents the southern motion of this same interface.

$$fu = -g^* \frac{\partial h}{\partial y} + \tau^y/\rho_o h_1 \tag{63}$$

Cross differentiating (62) and (63) yields

$$f\left(\frac{\partial u}{\partial x} + \frac{\partial v}{\partial y}\right) = \left(\frac{\partial \tau^y}{\partial x} - \frac{\partial \tau^x}{\partial y}\right)/\rho_o h_1 \tag{64}$$

Eliminating the divergence between (61) and (62) we have

$$\frac{\partial}{\partial t}(\Delta H) = \text{curl } \underset{\sim}{\tau}/\rho_o f \tag{65}$$

where $\frac{\partial}{\partial t}(\Delta H)$ is positive, because the curl of the wind stress is positive

A suitable estimation of ΔH is then

$$\Delta H = \frac{\int_o^t \text{curl } \underset{\sim}{\tau}\, dt}{\rho_o f} \tag{66}$$

By simple kinematics, $dt = dx/S$, where S represents the cyclone's speed. Therefore (66) may be expressed as

$$\Delta H = \frac{\int \text{curl } \underset{\sim}{\tau}\, dx}{\rho_o f S} \tag{67}$$

By introducing the values used in the model, an approximate value of ΔH is 10 meters. This estimate of ΔH agrees with the values observed in Fig. 5c.

The linear inviscid momentum equations have the form:

$$\frac{\partial u}{\partial t} = fv - g^* \partial h/\partial x \tag{68}$$

$$\frac{\partial v}{\partial t} = -fu - g^* \partial h/\partial y \tag{69}$$

The perturbation field is decomposed into a mean meridional component, denoted by $(\bar{})$ and a wave meridional structure, denoted by $(\tilde{})$. It is observed from figures 5a, b and c that the u and h solutions are in phase and that the u and v solution are in quadrature. Thus, the perturbation field is chosen to have the following solutions:

$$u = \bar{U}(y) + \tilde{U}(y) \cos\psi \tag{70}$$

$$v = \bar{V}(y) + \tilde{V}(y) \sin\psi \tag{71}$$

$$h = \bar{H}(y) + \tilde{H}(y) \cos\psi \tag{72}$$

where the phase, ψ, is equal to $kx - \omega t$. The zonal wavenumber , k, and the frequency, ω, are both positive quantities for a perturbation moving eastward at the wake of the cyclone. Introducing (70) - (72) into (68) and (69) yields

$$-\omega \tilde{U}\sin\psi - f(\bar{V}+\tilde{V}\sin\psi) = g^* k\tilde{H}\sin\psi \tag{73}$$

$$\omega \tilde{V}\cos\psi + f(\bar{U}+\tilde{U}\cos\psi) = -g^*\frac{d\bar{H}}{dy} - g^*\frac{d\tilde{H}}{dy}\cos\psi \tag{74}$$

Subtracting the mean values, over a period of the wave, allows us to decompose (73) and (74) into the following expressions:

$$\bar{V} = 0 \tag{75}$$

$$-\omega\tilde{U} - f\tilde{V} = g^*k\tilde{H} \tag{76}$$

$$f\bar{U} = -g^*\frac{d\bar{H}}{dy} \tag{77}$$

$$\omega\tilde{V} + f\tilde{U} = -g^*\frac{d\tilde{H}}{dy}\cos\psi \tag{78}$$

As shown by (75), the v perturbation solution has no mean meridional structure. This is confirmed in Figure (5b) where only the wave meridional structure is observed. Because the minimum value of h is

observed at the front, its meridional derivative is zero. Therefore:

$$\frac{d\tilde{H}}{dy} = 0 \tag{79}$$

From (78) it is inferred that $\tilde{V}$ and $\tilde{U}$ have opposite signs. Therefore, it may be concluded that the u perturbation solution leads the v perturbation solution by a quarter of a period. On the other hand, combining (78) with (76) yields:

$$\omega\left(\frac{f^2}{\omega^2} - 1\right) \tilde{U} = g^* k \tilde{H} \tag{80}$$

As f is greater than ω, both coefficients of $\tilde{U}$ and $\tilde{H}$ are positive. It follows immediately that the u perturbation solution is in phase with the h perturbation solution. This result is confirmed in Figs. 5a and 5c.

It is interesting to have an idea of the order of magnitude of the southward drift of the subarctic front. Fig. 6 gives us a schematic representation, in the (y, z) plane, of the initial position of the front and its location after a time Δt. By definition:

$$h_j = h_{jo} - \Delta h_j \tanh\left(\frac{y-W/2}{L_y}\right) \tag{81}$$

Therefore

$$\frac{dh}{dy}(y=W/2) = \frac{\Delta h_j}{L_y} \tag{82}$$

This value of $\frac{dh}{dy}$ is exactly equal to $\tan\varepsilon$. On the other hand, from Fig. 6 it is deduced that the value of $\tan\varepsilon$ is equal to the quotient of the amplitude of the vertical displacement of the interface.

Fig. 6 it is deduced that the value of $\tan\varepsilon$ is equal to the quotient of the amplitude of the vertical displacement of the interface, approximately 10 meters, by the southward shift of the front. By simple

calculations, it follows that the value of the southward shift is of the order of 10 kms. In this particular case, this is precisely the value of the width of the front.

At the end of the sixth day the center of the cyclone is located in the middle of the region of interest. Figure 7 shows the wave forced by the storm's passage propagating towards the eastern boundary. The most interesting feature to be observed is that the amplitude of the wave is exactly the same at all depths. Furthermore, no phase shift with depth is observed.

Geisler's theory predicts that very far to the rear of the storm, after the dispersion of the inertial gravity waves, the motion will be in geostrophic balance. This is understandable. In the absence of externally driven forces, the kinetic energy in the ocean will be redistributed. This feature is observed nine days later. However, one feature remains unalterable: the upward lifting of the four interfaces (Fig. 8). It is expected that this upwelled region will remain for several weeks after the passage of the storm.

A way of quantifying the dissipation of kinetic energy after the storm's passage is devised. For this purpose, the function

$$D = D_0 \exp(-t/\tau) \tag{83}$$

is approximated by the least square method. Here D represents the maximum depth variation of the first interface; D_0, the initial amplitude; t, time, and τ, the e-folding time scale. The constants to be determined by the least square method are $\ell n D_0$ and $-1/\tau$. Values of D are evaluated daily from the seventh to the fifteenth day. The values of $\ell n D$ versus time are plotted (Figure 9). The resulting value of τ is of the

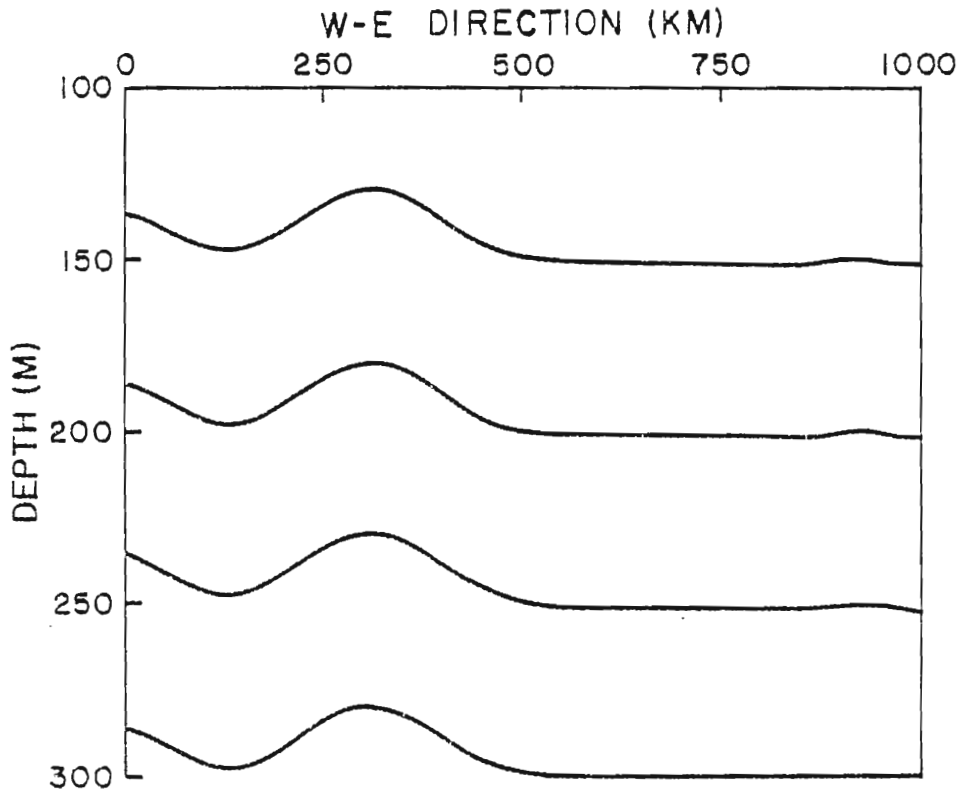

Figure 7. Cross section of the subarctic front in the (x, z) plane for the first cyclonic case after 6 days.

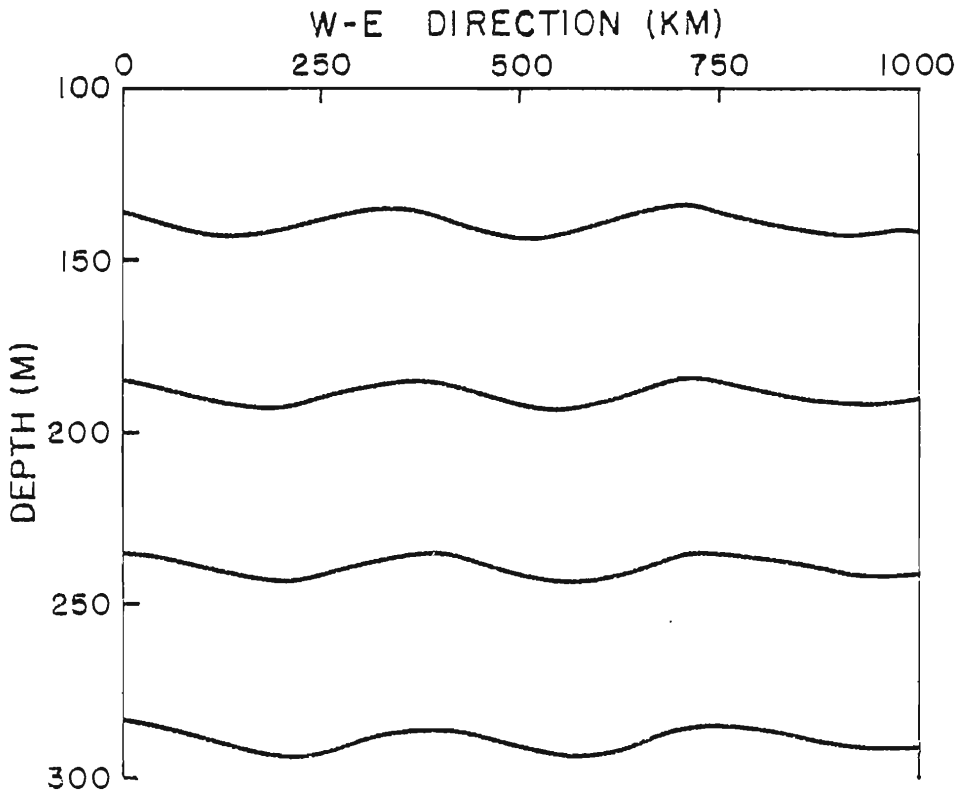

Figure 8. Same as Figure 7 but after 15 days.

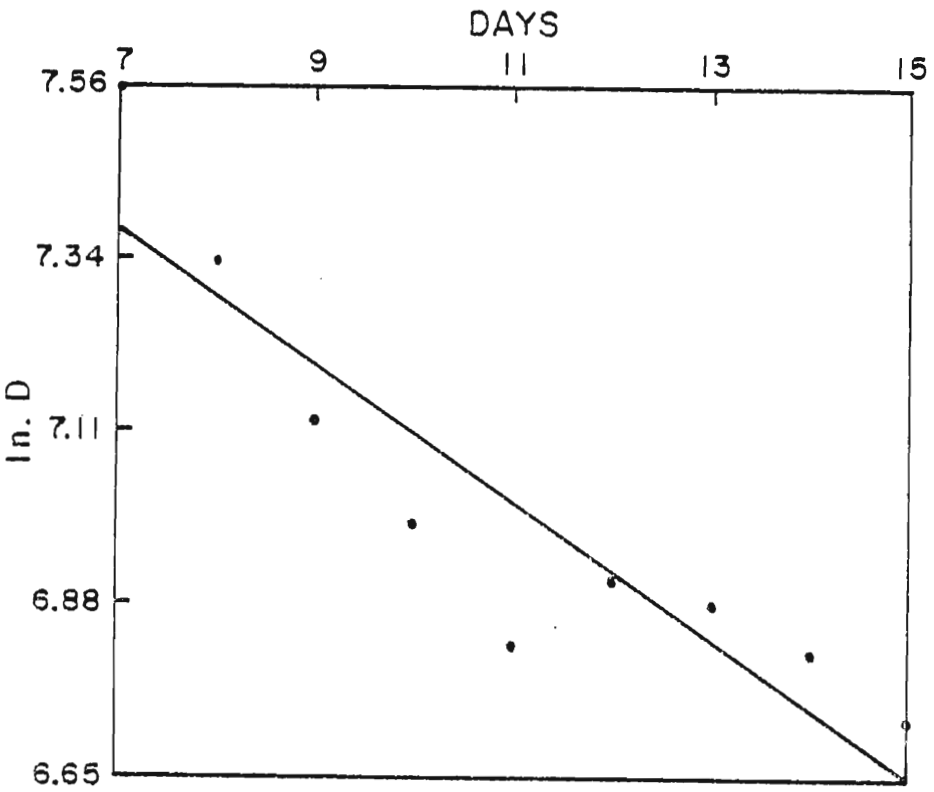

Figure 9. Decay in time of the amplitude of the vertical oscillation induced at the lee of the cyclone's track. While the dot points represent the original values of ln D (see text), the solid line represents the curve obtained by using the least square method in (83).

order of 10 days. This relatively short e-folding time scale confirms the fact that because of the absence of any external atmospheric wind forcing, the kinetic energy in the ocean is rapidly redistributed. A shorter e-folding time scale is to be expected if vertical mixing were to be included in the model.

Although the lee side of the storm is upwelled, a region of relative maximum convergence is observed in the lower layers below a region of maximum divergence in the upper layer (Figure 10a, b, c and d). The physical explanation of this phenomenon is quite simple. The water that is upwelled in the top layer tends to diverge to the meridional boundaries. Therefore, the cooler waters from the deeper layers tend to rise to the sea surface, generating a region of relative maximum convergence in the lower layers.

The initial position of the front in the (y, z) plane is depicted in Figure 11. While the water to the south of the figure represents the transition zone, the water to the north of the figure represents the subarctic zone. The subarctic front represents the natural boundary between these two zones. In the transition zone, located at the south of the front, the water is warmer and more saline that in the subarctic zone.

In our simulation, the center of the cyclone is travelling over the subarctic front from west to east. At the end of the seventh day two features are observed: the southward drift of the front and a local uplifting of the density interface (Fig. 12). Because of the β-effect, the cross-front velocity is more intense at the southern part of the

uplifting of the density interface (Fig. 12). Because of the β-effect, the cross-front velocity is more intense at the southern part of the

cyclone. Thus, the Ekman flow divergence will be lesser at the northern

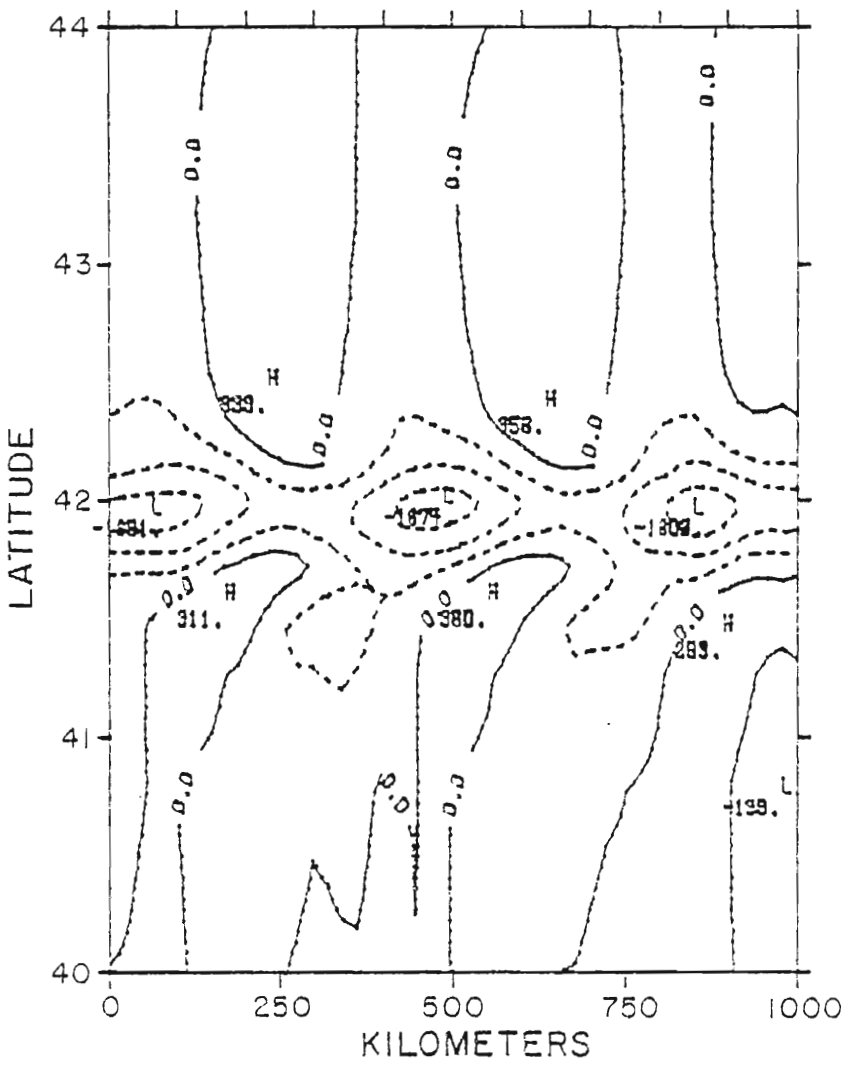

(a)

Figure 10. Isoanomalies of the height field a) for the first; b) the second; c) the third; and d) for the fourth layers, for the case of the cyclone travelling from west to east after 10 days.

Figure 10. Isoanomalies of the height field a) for the first; b) the second; c) the third; and d) for the fourth layers, for the case of the cyclone travelling from west to east after 10 days.

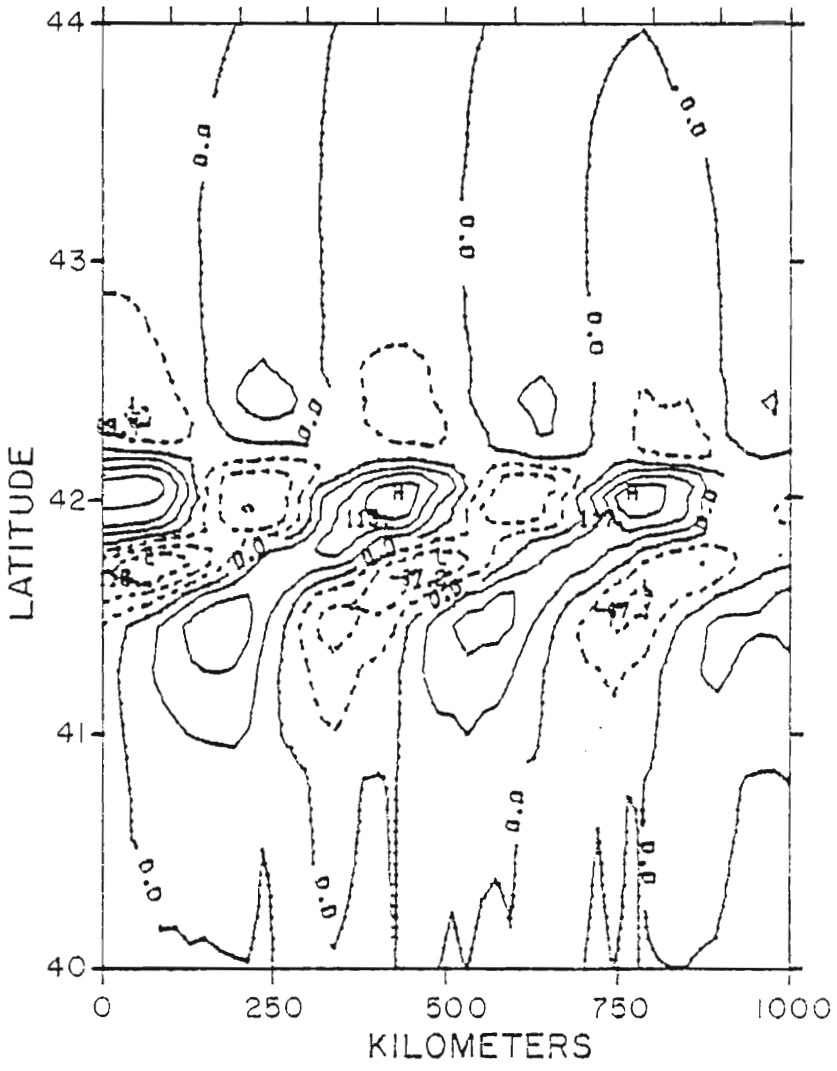

(b)

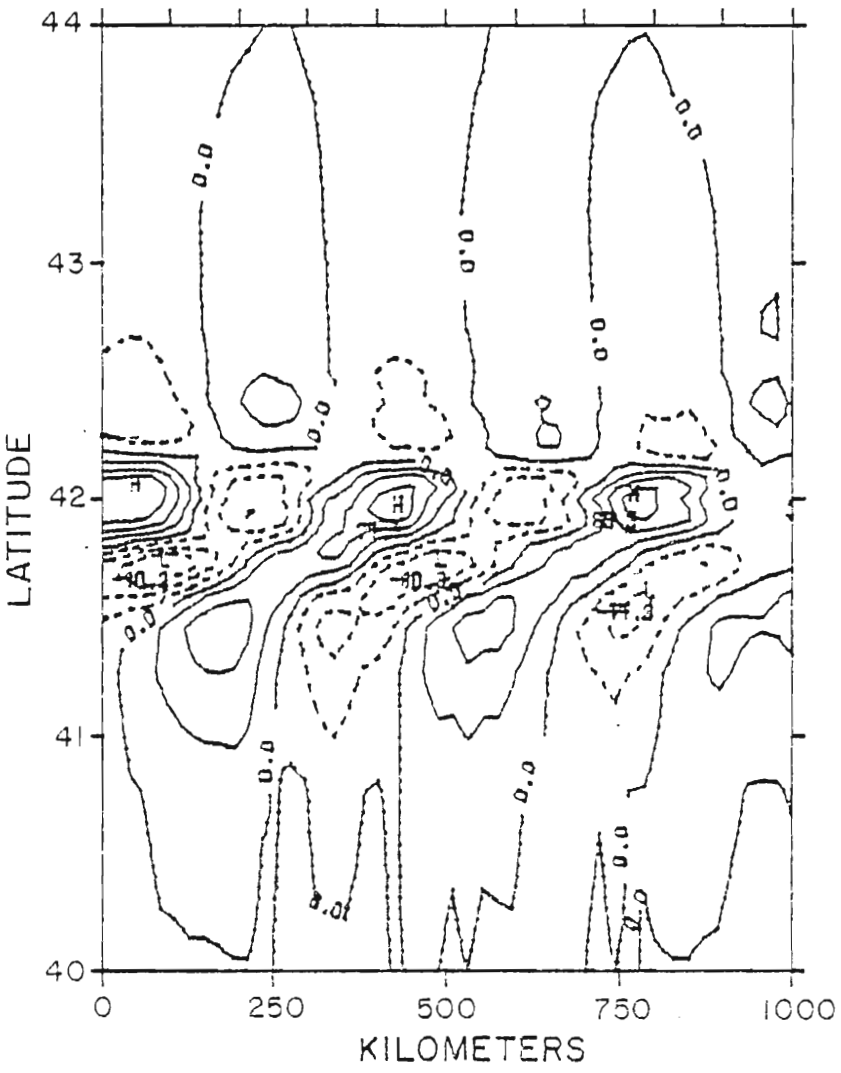

(c)

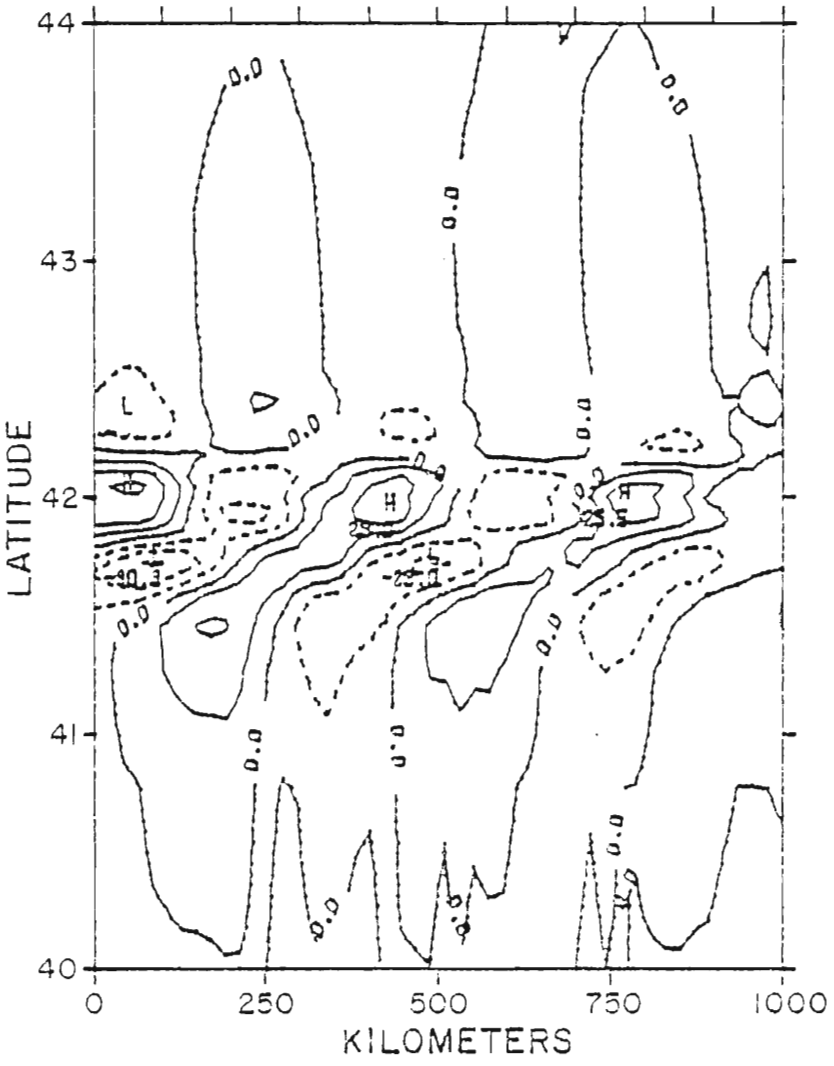

(d)

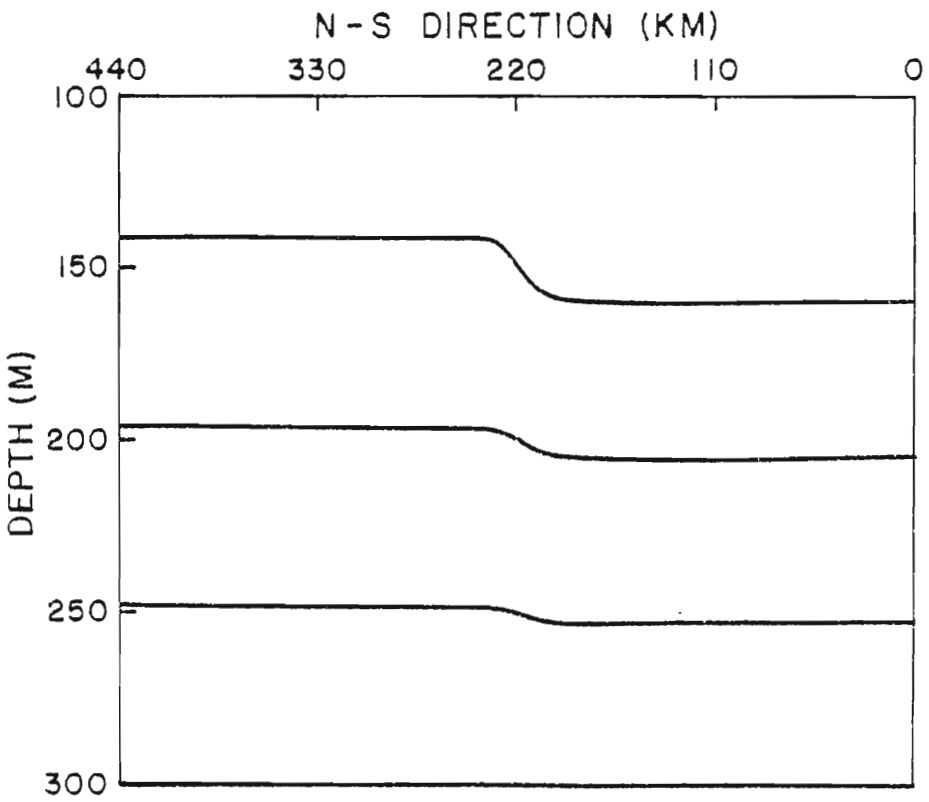

Figure 11. Initial position of the subarctic front in the (y, z) plane.

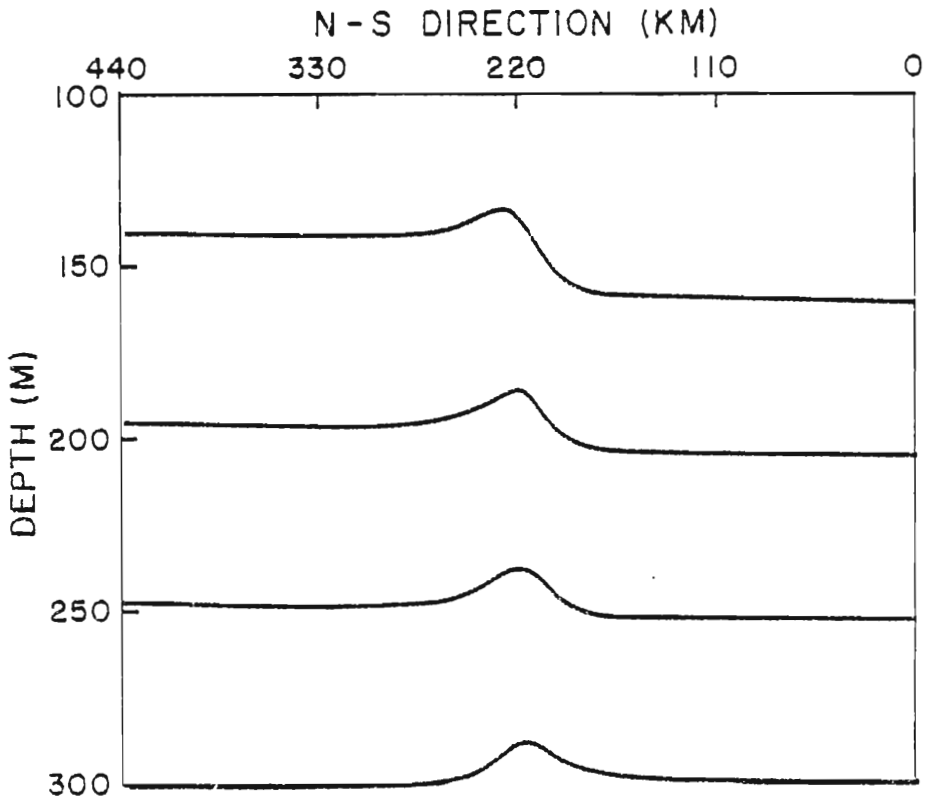

Figure 12. Cross section of the subarctic front in the (y, z) plane for the first cyclonic case after 7 days.

part of the front. This phenomenon explains the slight southward shift of the subarctic front. This particular form of upwelling is generated by the geometrical form of the cyclone. An intensification of the front is also observed.

On the other hand, the bump observed in Fig. 12 is generated by an upwelling of different origin. This upwelling is driven by the divergent Ekman flow generated by the counterclockwise motion of the cyclone. Using (65), an attempt to estimate the height of the bump is made. Recalling that S is the storm speed, an approximate estimate of the bump height, Δh, will be

$$\Delta h = \frac{\rho_a c_D V_o^2}{S f \rho_o} \tag{84}$$

$$= 20 \text{ meters}$$

Thus, the bump caused by the Ekman flow has an approximate height of 20 meters.

In general, a decrease of temperature is observed at the wake of the cyclone. The magnitude of the temperature decrease is directly related to both the magnitude and the speed of the cyclone. Because our model does not allow vertical mixing, the fresher and cooler waters from beneath cannot reach the sea surface. Therefore, the temperature field of the top layer will remain almost unaltered. However, a slight southward shift of the salinity and the temperature fronts in the upper layer is detected nine days after the cyclone's passage.

To study the effects caused by the latitudinal change, a cyclone travelling from north to south is considered. To make comparisons

To study the effects caused by the latitudinal change, a cyclone travelling from north to south is considered. To make comparisons
easier, the stress and speed of this cyclone will remain the same as in the previous case.

In the present case, the outer basin has an extension of 5900 and 1000 kilometers in the meridional and latitudinal directions, respectively. On the other hand, the inner mesh has a width of 1000 kilometers and a length of 200 kilometers. The northern inner boundary is located 1500 kilometers to the south of the northern outer boundary.

Initially located at 5900 kilometers north of the equator, the cyclone travels along the y axis at a speed of 500 kilometers per day. It reaches the northern inner boundary at the end of the second day.

At the end of the fourth day, the center of the cyclone is located in the middle of the southern inner boundary. Essentially, the principal features are recovered, as energy remains concentrated in a somewhat wider strip at the wake of the storm (Fig. 13). This phenomenon should be attributed to the increasing value of the baroclinic radius of deformation, which is inversely proportional to f.

It is observed that the region of maximum uplifting is biased more to the right and lags the center of the cyclone by a distance of almost 300 kilometers. The amplitude of the water uplifted is greater, in the present case, by almost a factor of 2. This result is consistent with Geisler's (1970) theory in the sense that it predicts a displacement of the thermocline, in the wake of the cyclone, inversely proportional to f^3.

The wave along the track has a wavelength of 500 km, which is greater than in the previous case. Again, this result is also consistent with Geisler's theory, which predicts that the wavelength should be

with Geisler's theory, which predicts that the wavelength should be

inversely proportional to f.

2) The water remains upwelled for several weeks.

3) An intensification of the subarctic front takes place.

4) A southward shift of the subarctic front is observed.

5) A region of relative maximum convergence is observed in the lower layers below a region of maximum upwelling in the upper layer.

6) The u and v fields are in quadrature in space with the v field leading the u field.

7) Energy is concentrated to a narrow strip at the wake of the storm. The result agrees with Geisler's linear theory.

The simulation of the westerly atmospheric winds shows a southward drift of the front due to the southerly Ekman flow. While the passage of an atmospheric cold front does not play any significant role in the dynamical structure of the subarctic front, the simulation of the curl shows the classical convergence that strongly favors frontogenesis in that region.

Two initial forms of oceanic fronts are considered. The results, in all the cases tested, are very conclusive: the frontal response to the different atmospheric wind forcings is independent of the initial form of the subarctic front.

APPENDICES

A. ON THE EIGENVALUE PROBLEM

During the course of this research, it was verified that if the jump in density between layers remains constant, the numerical model becomes numerically unstable. The problem is traditionally overcome by changing the constancy in the density jump between layers (McNider and O'Brien, 1973). However, a deeper understanding is required. To achieve this goal, the phase speed of the first baroclinic mode is evaluated.

To accomplish this task, a linearized version of the non-viscous model equation is sufficient. Such a linearized version of the momentum equations is

$$\frac{\partial u^j}{\partial t} - fv^j = -g \sum_{i=1}^{4} \left(\frac{\rho_5 - \rho_\nu}{\rho_j}\right) \frac{\partial h_i}{\partial x} \tag{A.1}$$

$$\frac{\partial v^j}{\partial t} + fu^j = -g \sum_{i=1}^{4} \left(\frac{\rho_5 - \rho_\nu}{\rho_j}\right) \frac{\partial h_i}{\partial y} \tag{A.2}$$

where the superscript j goes from 1 at the top to 5 at the bottom, and again ν is the maximum value of the pair (i, j). The linear form of the continuity equation leads to

$$\frac{\partial h^j}{\partial t} + H^j\left(\frac{\partial u^j}{\partial x} + \frac{\partial v^j}{\partial y}\right) = 0 \tag{A.3}$$

where H^j represents the mean depth of the j-th layer. The differentiation of (A.1) with respect to time yields

$$\frac{\partial^2 u^j}{\partial t^2} - f\frac{\partial v^j}{\partial t} = -g \sum_{i=1}^{4} \left[\left(\frac{\rho_5 - \rho_\nu}{\rho_j}\right) \frac{\partial}{\partial x}\left(\frac{\partial h_i}{\partial t}\right)\right] \tag{A.4}$$

Introducing (A.3) into this last expression yields

$$\frac{\partial^2 u^j}{\partial t^2} - f\frac{\partial v^j}{\partial t} = -g\sum_{k=1}^{4}\left[\left(\frac{\rho_5-\rho_\nu}{\rho_j}\right) H_k \left(\frac{\partial^2 u_k}{\partial x^2} + \frac{\partial^2 u_k}{\partial x \partial y}\right)\right] \tag{A.5}$$

This set of equations is coupled. To decouple (A.5), u^j and v^j can be decomposed into its vertical modes in the following manner:

$$()^j = \sum_{k=1}^{5} c_k^{\,j}\,(\tilde{\ })_k \tag{A.6}$$

where the value k = 5 corresponds to the barotropic mode while k = 1,2,3 and 4 represents the four possible baroclinic modes. On the other hand, $c_k{}^j$ and u_k represent the eigenvector and the amplitude of the k-th mode, respectively.

The elements of a certain matrix N_{kj} may be defined in the form

$$N_{kj} = gH_k\left(\frac{\rho_5-\rho_\nu}{\rho_j}\right) \tag{A.7}$$

Upon substitution of (A.6) and (A.7) in (A.5), a single expression for each mode is obtained:

$$c_k{}^j\left(\frac{\partial^2 \tilde{u}_k}{\partial t^2} - f\frac{\partial \tilde{v}_k}{\partial t}\right) = \sum_{k=1}^{5} N_{kj}\, c_k{}^j\left(\frac{\partial^2 \tilde{u}_k}{\partial x^2} + \frac{\partial^2 \tilde{u}_k}{\partial x \partial y}\right) \tag{A.8}$$

The set of equations is no longer coupled. Because $c_k^{\,j}$ is an eigenvector of the matrix N_{kj}, it must satisfy the relation

$$\sum_{k=1}^{5} N_{kj}\, c_k^{\,j} = \sigma_k c_k^{\,j} \tag{A.9}$$

where σ_k is the associated eigenvalue. Using (A.9) in (A.8) a final expression for the linear u momentum equation is

where σ_k is the associated eigenvalue. Using (A.9) in (A.8) a final expression for the linear u momentum equation is

$$\frac{\partial^2 \tilde{u}_k}{\partial t^2} - f\frac{\partial \tilde{v}_k}{\partial t} = \sigma_k\left(\frac{\partial^2 \tilde{u}_k}{\partial x^2} + \frac{\partial^2 \tilde{u}_k}{\partial x \partial y}\right) \tag{A.10}$$

Proceeding in the same manner, a similar expression may be derived for the v momentum equation:

$$\frac{\partial^2 \tilde{v}_k}{\partial t^2} + f \frac{\partial \tilde{u}_k}{\partial t} = \sigma_k \left(\frac{\partial^2 \tilde{v}_k}{\partial x \partial y} + \frac{\partial^2 \tilde{v}_k}{\partial y^2}\right) \tag{A.11}$$

From (A.7) it follows that the elements N_{5j} and N_{k5} are identically zero. This result should be no surprise as the barotropic mode has been filtered out. It is convenient to define a matrix M_{kj} which is related to the matrix N_{kj} by the form

$$M_{kj} = N_{k-1\ j-1} \tag{A.12}$$

where k and j vary from one to four in M_{kj}.

The next task is to evaluate the eigenvalues of the first baroclinic mode. Two cases are considered. In one case the densities are arbitrarily chosen to be $\rho_1 = 1.000$, $\rho_2 = 1.002$, $\rho_3 = 1.0022$, $\rho_4 = 1.0025$ and $\rho_5 = 1.0027$ g cm^{-3}. In the other case, the density jump between layers is constant from layer to layer. Thus, $\rho_1 = 1.000$ g cm^{-3}, $\rho_{1+i} = \rho_1 + i\Delta\rho_i$ where $i = 1(1)4$ and $\Delta\rho_i = 10^{-3}$. In both cases, the layer depths are

$$\begin{aligned} H_1 &= mk \\ H_2 &= nk \\ H_3 &= H_4 = k \end{aligned} \tag{A.13}$$

where k = 50 meters and m and n are allowed to vary alternatively from one to three. In all the different tests conducted, the eigenvalues of the first baroclinic mode proved to be larger in the case of equal jump one to three. In all the different tests conducted, the eigenvalues of the first baroclinic mode proved to be larger in the case of equal jump in density. That difference ranged between 80% and 140%. (Table 3)

The phase speed is equal to the square root of the eigenvalue of the respective baroclinic mode. Therefore, the phase speed of the first baroclinic mode is larger for the case where the jump in density is constant. It is immediately conclusive from the CFL criterion for numerical instability that a smaller time step, Δt, for this case is required. This result was confirmed in all the model runs tested. In particular, the time step used in the numerical model is 20% larger than the one which would be needed if an equal density jump between layers were used.

H_1 \ H_2	1	2	3
1	14388.9	14859.0	15886.9
2	27678.5	27800.8	27973.7
3	41124.3	41191.5	41273.7

(a)

H_1 \ H_2	1	2	3
1	34534.3	44855.7	57612.9
2	50452.5	56025.1	64769.9
3	68917.0	72054.1	77099.3

(b)

Table 3. Eigenvalues of the first baroclinic mode for $H_1 = mK$, and $H_2 = nK$, where m and n varies from 1 to 3 and, when: a) $\rho_1 = 1.0$; $\rho_2 = 1.002$; $\rho_3 = 1.0022$; $\rho_4 = 1.0025$; $\rho_5 = 1.0027$ g cm^{-3}; b) $\rho_{1+i} = \rho_1 + i\Delta\rho_i$, where i = 1(1)4 and $\Delta\rho_i = 10^{-3}$ g cm^{-3}.

B. ON THE BAROTROPIC INSTABILITY OF THE SUBARCTIC FRONT

The phenomenon by which eddies are generated by horizontal shear in the mean flow is known as barotropic instability. In this case, eddies may extract energy from the mean flow kinetic energy. However, the mean flow may also extract energy from the mean potential energy field. Therefore, in the case of barotropic instability, energy may be supplied by the mean potential energy field.

Kuo (1949) studied the stability of a horizontal, rotating, non-divergent flow. In doing so, he extended Lord Rayleigh's (1880) theorem for a non-rotating system. Kuo proved the necessary condition for barotropic instability, by which the gradient of absolute vorticity must change sign at least once along the meridional extension of the basin being considered.

The aim of the present work is to derive a stability criterion for a geostrophically balanced upper oceanic front. To accomplish this thrust, a two-layer model is considered, in such a way, that the lower layer is chosen to be infinitely deep. To simplify the complexity of the equations to be used, the following hypotheses are made:

1) the oceanic front is geostrophically balanced; i.e., $-f\bar{u} = g^* \frac{\partial \bar{h}}{\partial y}$, $\bar{v} = 0$, where g^* represents the reduced gravity and the over-bar ($\bar{}$) quantities represent the basic state;

2) because the meridional extent of the oceanic front, L_y, is of the order of thirty kilometers, the f-plane approximation is used;

3) the zonal wavenumber , k, is much smaller than $(L_y)^{-1}$; therefore only long waves are considered;

4) the vorticity at the front, represented by $-\partial\bar{u}/\partial y$, is much less than the planetary vorticity, f.

The linear inviscid perturbation equations for a single-layer fluid may be written as

$$\frac{\partial u'}{\partial t} + \bar{u}\frac{\partial u'}{\partial x} + v'\frac{\partial \bar{u}}{\partial y} - fv' = -g^*\frac{\partial h'}{\partial x} \qquad \text{(B-1)}$$

$$\frac{\partial v'}{\partial t} + \bar{u}\frac{\partial v'}{\partial x} + fu' = -g^*\frac{\partial h'}{\partial y} \qquad \text{(B-2)}$$

$$\frac{\partial h'}{\partial t} + \bar{h}\frac{\partial u'}{\partial x} + \bar{u}\frac{\partial h'}{\partial x} + v'\frac{\partial \bar{h}}{\partial y} + \bar{h}\frac{\partial v'}{\partial y} = 0 \qquad \text{(B-3)}$$

where the prime quantities represent the perturbation. In (B-2) the geostrophic balance is substracted.

Assuming that the perturbation quantities have a wavelike form

$$\begin{Bmatrix} u' \\ v' \\ h' \end{Bmatrix} = \begin{Bmatrix} U(y) \\ V(y) \\ H(y) \end{Bmatrix} \exp\,[ik(x-ct)] \qquad \text{(B-4)}$$

where U(y), V(y) and H(y) are respectively the amplitudes of u', v' and h', the above set of equations has the form

$$ik(\bar{u}-c)U + \left(\frac{d\bar{u}}{dy} - f\right)V = -g^*\, ikH \qquad \text{(B-5)}$$

$$fU + ik(\bar{u}-c)\,V = -g^*\, dH/dy \qquad \text{(B-6)}$$

$$ik\bar{h}U + \frac{d}{dy}(\bar{h}V) + ik(\bar{u}-c) = 0 \qquad \text{(B-7)}$$

$$ik\bar{h}U + \frac{d}{dy}(\bar{h}V) + ik(\bar{u}-c) = 0 \qquad \text{(B-7)}$$

This system of equations may be reduced, after some algebraic manipulations, to the single equation

$$(\bar{h}H')' - \left[\frac{f\bar{h}'}{\bar{u}-c} + \frac{(\bar{h}\bar{u}')'}{\bar{u}-c} + \alpha^2\bar{h}\right] H = 0 \qquad \text{(B-8)}$$

where $\alpha^2 = f^2(g^*\bar{h})^{-1}$ is the inverse of the Rossby radius of deformation squared.

Since the meridional length scale we are interested in is of the order of thirty kilometers, it may be assumed that $H(\infty) = H(-\infty) = 0$.

For this type of perturbation to be unstable, the phase speed, $c(= c_r + ic_i)$, must be complex. The amplitude functions must also be complex.

For the sake of simplicity, the variable $Z(= \bar{u}-c)$ is introduced, and the following change of variables is made (Howard, 1961): $H = Z^{\frac{1}{2}} Q$. With these considerations, (B-8) may be expressed as

$$(\bar{h}ZQ')' - \left[f\bar{h}' + \frac{1}{2}(\bar{h}'\bar{u}')' + \alpha^2\bar{h}Z + \frac{\overline{hu}'^2}{4Z}\right]Q = 0 \qquad \text{(B-9)}$$

Multiplying (B-9) by Q^* and upon integration by parts yields

$$\int\left\{\bar{h}Z|Q'|^2 + \left[f\bar{h}' + \frac{1}{2}(\bar{h}'\bar{u}')' + \alpha^2\bar{h}Z + \frac{\overline{hu}'^2}{4Z}\right]|Q|^2\right\}dy = 0 \qquad \text{(B-10)}$$

where the limits are omitted.

The imaginary part of Z is $-c_i$. It follows immediately that the imaginary part of Z^{-1} is $-c_i|Z|^{-2}$. Therefore, the imaginary part of (B-10) yields

$$c_i\int\left[\bar{h}|Q'|^2 + \left\{\alpha^2\bar{h} - \frac{\overline{hu}'^2}{4|Z|^2}\right\}|Q|^2\right]dy = 0 \qquad \text{(B-11)}$$

Whenever

$$4|Z|^2 > \overline{hu}'^2$$

Whenever

$$|Z|^2 = |\bar{u}-c|^2 > R^2 = \frac{g^*\overline{hu}'^2}{4f^2} \qquad \text{(B-12)}$$

the integrand of (B-11) has a positive definite form. In such a case, (B-11) holds only if $c_i = 0$. If the condition (B-12) is satisfied, then for a given phase speed c for every point along the front, the stability of the front to the fluctuation is guaranteed.

Looking at the problem from a mathematical point of view, criterion (B-12) is met outside the circle of radius R centered at $(\overline{u}, o)$ along the c_r axis. For a given oceanic front, both $\overline{h}$ and $\overline{u}$ are functions of the latitude, y. Therefore, for every latitudinal point, y, across the front there corresponds one interval and one radius.

The two extremes - maximum and minimum - of this family of intervals delimit the region of stability. In other words, any point outside that region corresponds to a stable fluctuation of the front. This is a sufficient condition of stability.

What follows is an attempt to apply this stability criterion to an upper oceanic front. For the sake of generality, let us define the depth of the upper layer, $\overline{h}$, via a hyperbolic tangent, in such a way that

$$\overline{h} = \overline{h}_{oo} - \Delta h \tanh(y/L_y) \qquad \text{(B-13)}$$

where $\overline{h}_{oo}(\Delta h)$ represents the mean value (amplitude) of the upper layer. For this steady oceanic front to subsist, the interface, $\overline{h}$, must be balanced initially by a zonal velocity of the form

$$\overline{u} = -(g^*/f)\left(\frac{\partial \overline{h}}{\partial y}\right) \qquad \text{(B-14)}$$

By continuity, the meridional velocity, $\overline{v}$, is initially set to be zero.

It is convenient here to non-dimensionalize the governing equations.
By continuity, the meridional velocity, $\overline{v}$, is initially set to be zero.

It is convenient here to non-dimensionalize the governing equations.
Let y be scaled by L_y, ω by f, k by α and $\overline{u}$ and c by the zonal velocity

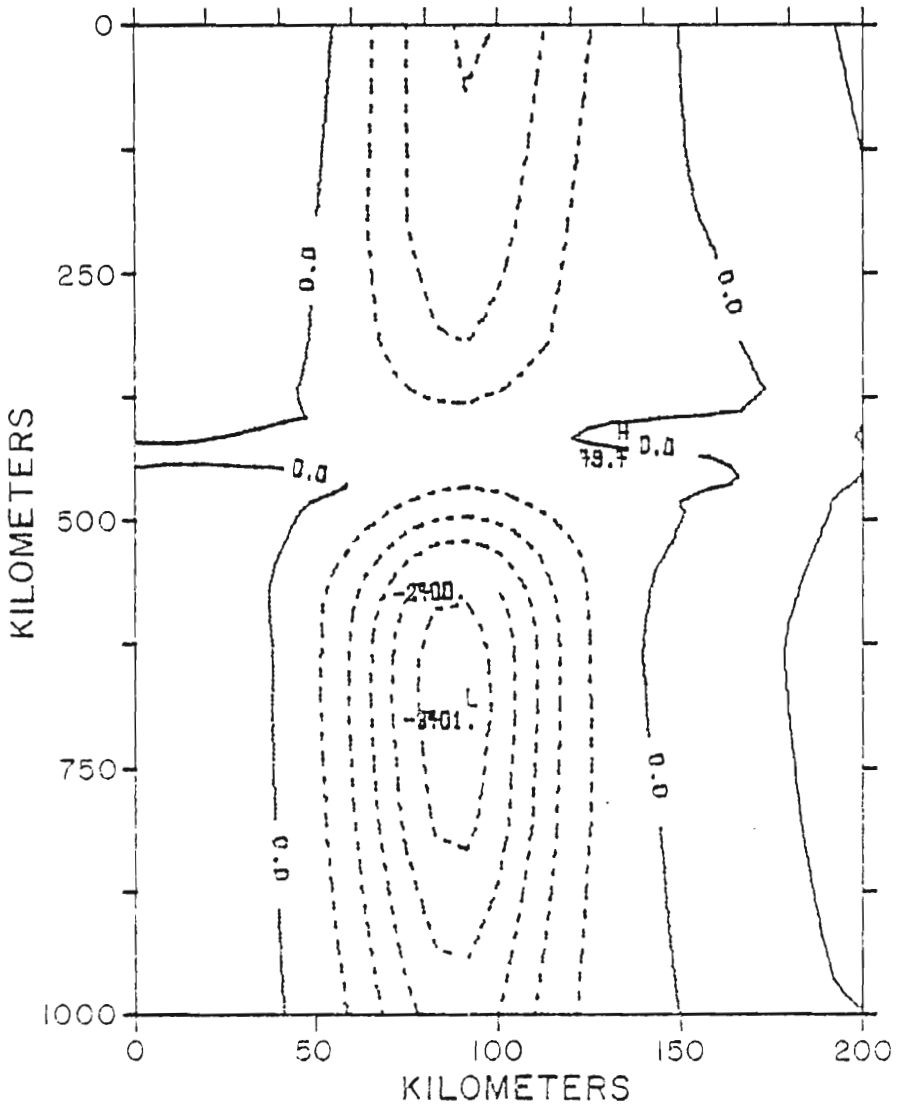

Figure 13. Isoanomalies of the height field of the top layer for the cyclone travelling from north to south, after 4 days.

An east-west cross section of the subarctic front one week after the cyclone had passed the front is shown in Figure 14. The main feature, i.e., water uplifted by 20 meters, is observed in the four layers. However, the maximum of water uplifted, in this case, is slightly biased to the west, i.e., to the right of the storm's track. This result is perfectly consistent with what is observed in the previous figure. The downwelling observed at both lateral boundaries may be explained by continuity. As upwelling persists one week after the cyclone's passage, the result previously obtained still holds; namely, that in the absence of any external dissipation, water will remain upwelled for several weeks.

On the other hand, a closer look at a north-south cross section of the subarctic front, shows that the features observed for the cyclone's case previously considered are recovered (Fig. 15), namely; an upwelling of around 20 meters of the four interfaces, a strengthening of the subarctic front, and a bump of around twenty meters at the site of the front. In the present case, it is observed that the southward drift of the front is more pronounced (of the order of 25 kilometers).

The oceanic frontal response to a severe atmospheric front is also considered. The atmospheric front is initially located at 1000 km to the west of the northwest corner of our region of interest (Fig. 16). With an angle of inclination of 45° with respect to the latitudinal circles, the atmospheric front moves in a direction perpendicular to its axis of orientation. Travelling at a speed of 500 kilometers per day, it reaches

the atmospheric front moves in a direction perpendicular to its axis of orientation. Travelling at a speed of 500 kilometers per day, it reaches the southwest corner after 51 hours. Although the northwesterly winds simulated behind the atmospheric front are severe, no significant

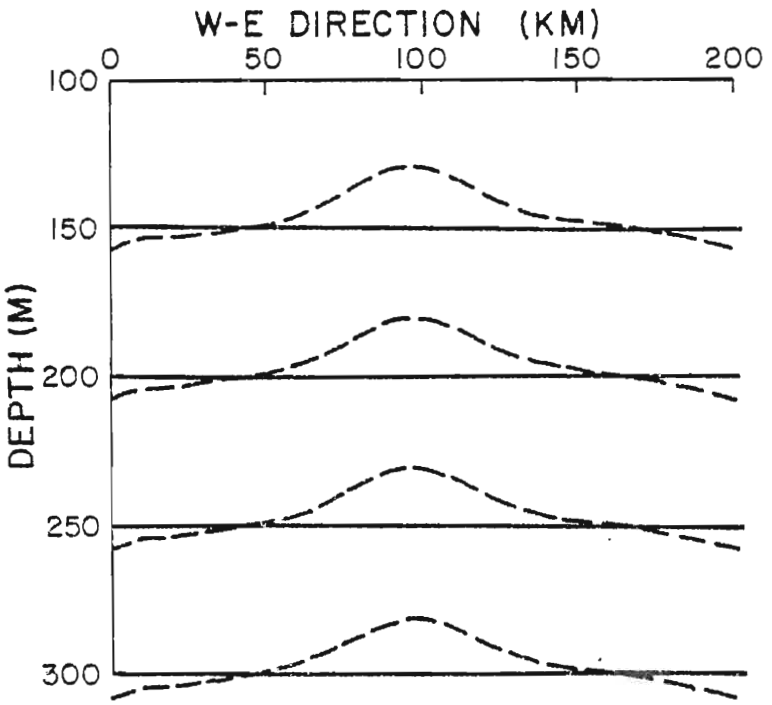

Figure 14. Cross section of the subarctic front in the (x, z) plane for the second cyclonic case. The solid line represents the initial position of the density interfaces, while the dashed line represents the position of the interfaces after 10 days.

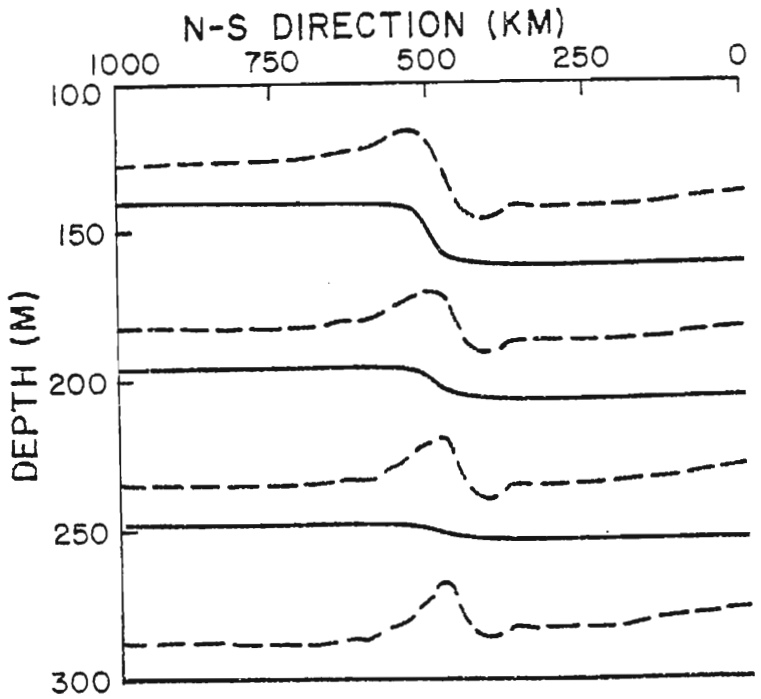

Figure 15. Cross section of the subarctic front in the (y, z) plane for the second cyclonic case. The solid line represents the initial position of the density interfaces, while the dashed line represents the position of the interfaces after 10 days.

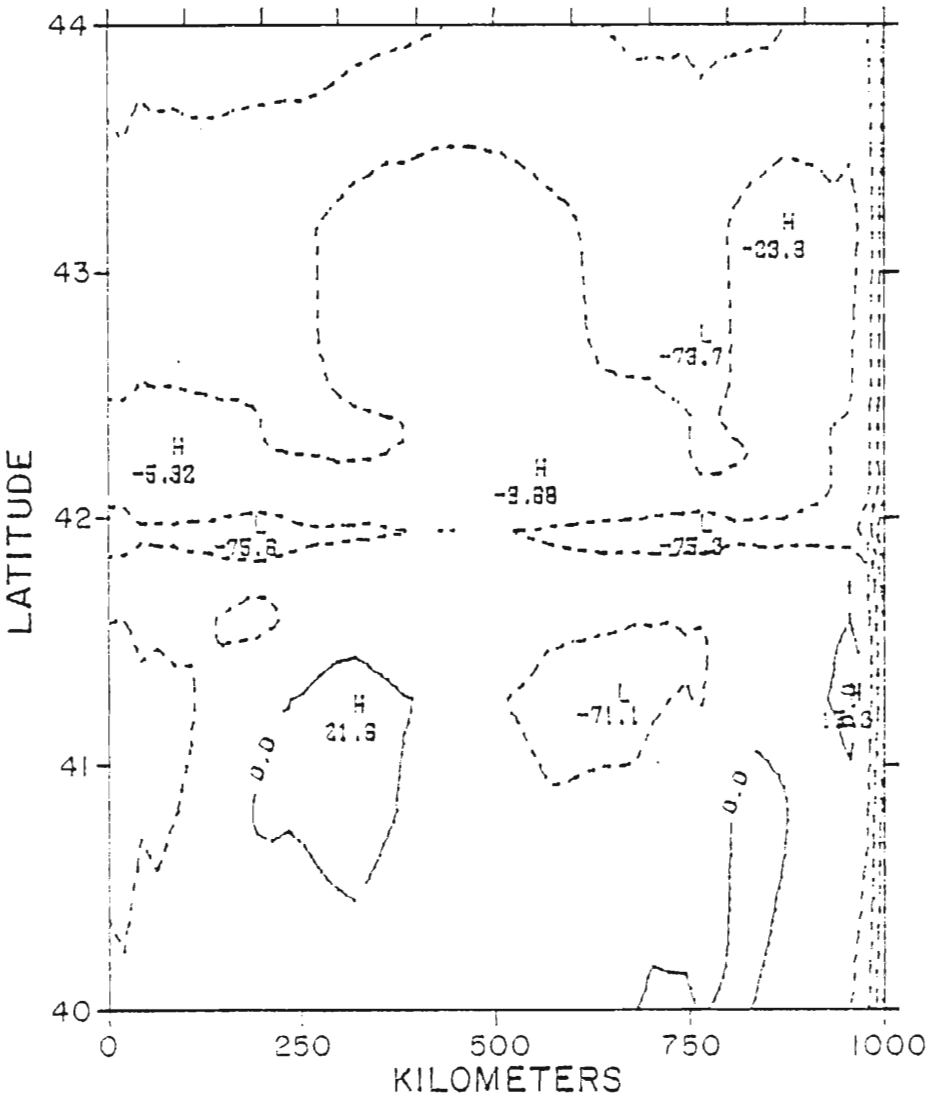

Figure 16. Isoanomalies of the height field of the top layer for the atmospheric front case after 10 days.

atmospheric front case after 10 days.

change in the height field is reported after 10 days (Fig. 16). Therefore, it can be concluded that the passage of an atmospheric front plays no significant role in the dynamics of the subarctic front.

The kind of atmospheric wind forcing that is implemented in this study is the one that is typically observed at the latitude of the subarctic front. In the first instance, the oceanic front is chosen to be parallel to the latitudinal circles. In order to make this study more comprehensive, an initial undulatory front is also simulated (Fig. 2). At first glance one would expect a similar response of both fronts to similar atmospheric wind forcing.

For the first type of oceanic front, whenever the westerly wind is simulated, upwelling is observed at the site of the front. Conversely, whenever a negative curl stress is simulated, convergence is observed at the site of the front. But perhaps the most exciting experiment represents the simulation of a moving cyclone. A strong upwelling, that remains for several weeks, is observed along the storm track. The results of this particular case agree very well with Geisler's linear theory.

The main result of this research is that the momentum transfer, in the case of the subarctic front, is confined to the first 150 meters. The only exception is represented by the travelling cyclone. Therefore, a good agreement with Roden's observations is achieved.

The existence of undulatory fronts is very frequent in the North Pacific Ocean. Therefore, an initial undulatory subarctic front is

The existence of undulatory fronts is very frequent in the North Pacific Ocean. Therefore, an initial undulatory subarctic front is simulated by a sinusoidal wave along the latitudinal circles (Fig. 2). The longitudinal wavelength, L_x, is chosen to be 500 kms, while the

meridional wave amplitude, L_y, is chosen to have a value of 10 kilometers. As our intention is to observe the waves propagate, no atmospheric forcing is imposed in the first model run. After ten days, the undulatory front remains unaltered.

The phase speed of a Rossby-gravity wave, c_R, is given by

$$c_R = \frac{-\beta}{k^2+\ell^2+f^2/g^*H} \tag{85}$$

With the values used in the numerical model, c_R will have an approximate value of 0.1 cm/sec. Therefore, the westward propagation of the Rossby wave will be of the order of one kilometer in ten days. This value explain the fact that no displacement of the front is observed.

Because the meridional extent of the front is small, the Rossby wave cannot propagate at an appreciable rate (see (85)). It can be concluded that the β-effect does not play any significant role in the dynamics of the subarctic front. Therefore, the f-plane approximation made in section 3 is perfectly consistent.

To make this study more complete the spectrum of experiments is broadened. The question to be answered is whether a different initial configuration of the oceanic front gives the same kind of dynamical response as in the case of the nonundulatory oceanic front. For this purpose, the same atmospheric wind forcings described before are simulated in the case of the undulatory front.

The response of the undulatory oceanic front to the passage of a

simulated in the case of the undulatory front.

The response of the undulatory oceanic front to the passage of a strong cyclone is addressed. The intention is to study the oceanic

response of two different initial configurations, using the same cyclonic wind forcing. To accomplish this task, only the height field solution is considered (Fig. 17). Comparison between figures 17 and 10a shows that the height field variations are identical in both fronts. The numerical simulation of the other atmospheric wind forcings, i.e., westerly winds, curl and atmospheric fronts, shows identical results in the isoanomal height field for both fronts.

It can be concluded that the frontal response to the different atmospheric wind forcings is independent of the initial configuration of an oceanic front.

response of two different initial configurations, using the same cyclonic wind forcing. To accomplish this task, only the height field solution is considered (Fig. 17). Comparison between figures 17 and 10a shows that the height field variations are identical in both fronts. The numerical simulation of the other atmospheric wind forcings, i.e., westerly winds, curl and atmospheric fronts, shows identical results in the isoanomal height field for both fronts.

It can be concluded that the frontal response to the different atmospheric wind forcings is independent of the initial configuration of an oceanic front.

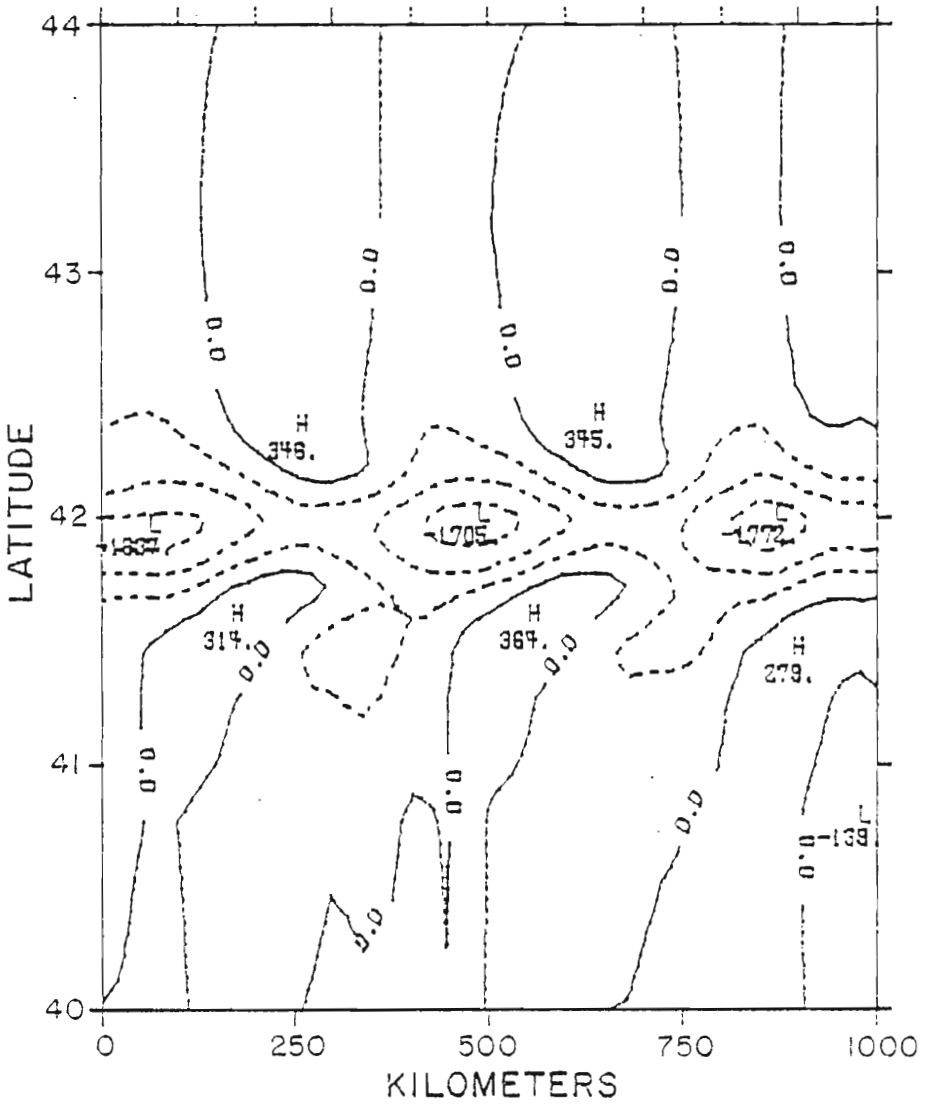

Figure 17. Isoanomalies of the height field of the upper layer of the undulatory front for the case of the cyclone travelling from west to east after 10 days.

undulatory front for the case of the cyclone travelling from west to east after 10 days.

5. SUMMARY AND CONCLUSIONS

A comprehensive theoretical and numerical study of the subarctic front has been performed. On the theoretical side, it has been established that horizontal friction plays no significant role as a mechanism of dissipation. A stability criterion has been established by which if $|\overline{u}-c|^2 > g^* h\overline{u}'^2/4f^2$ everywhere, the front is barotropically stable. In another theoretical attempt, the numerical instability caused by the constancy in the density jump between layers has been addressed.

The numerical aspect of this research consisted of a series of numerical simulations of different atmospheric wind forcings over the subarctic front. It has been established that the effects of the atmospheric wind forcing are confined to the first 150 meters. These results agree with Roden's observations in the sense that the dynamical response to the atmospheric forcing is limited to the layer between the sea surface and the high stability layer (which in the case of the subarctic front has an annual variation between 120 and 180 meters of depth). The only exception is represented by the passage of a strong cyclone, where an upwelling, of the order of 20 meters, of the four interfaces is observed at the wake of the cyclone. The following conclusions for this case can be drawn:

1) The e-folding time scale of the maximum depth variation of the first interface is of the order of 10 days. Thus, in the absence of external forcing, the kinetic energy is rapidly redistributed.

at the front, noted $|\overline{u}|_m$. The non-dimensional variables η, κ, χ, γ and μ are introduced as follows:

$$\eta = y/L_y \qquad \kappa = \omega/f$$
$$\gamma = c|\overline{u}|_m \qquad \chi = k/\alpha \tag{B-15}$$
$$\mu = \overline{u}/|\overline{u}|_m$$

The basic state may be rewritten as

$$\overline{h} = \overline{h}_{oo} - \Delta h \tanh \eta \tag{B-16}$$

$$\overline{u} = \frac{g^*}{f}\frac{\Delta h}{L_y} \operatorname{sech}^2 \eta \tag{B-17}$$

The expression for the zonal velocity at the front has the form

$$|\overline{u}|_m = \frac{g^*\Delta h}{fL_y} \tag{B-18}$$

By definition, it follows that μ will be equal to $\operatorname{sech}^2\eta$. Thus, the derivative of μ with respect to η has the form $-2 \tanh \eta \operatorname{sech}^2\eta$. With this formulation, criterion (B-12) has the final form

$$|\mu-\gamma|^2 \geq \frac{g^*h_{oo}}{f^2L_y^2}\left(1-\frac{\Delta h}{h_{oo}} \tanh \eta\right) \operatorname{sech}^4 \eta \tanh^2 \eta = \Phi^2 \tag{B-19}$$

For the purpose of clarity, a family of circles of radius Φ, each one centered at μ, is constructed in the complex γ plane (Fig. 18). The envelope defined by the family of circles delimits the outer region of stability. Because of the positive contribution of the term $hZ|Q'|^2$ in (B-11), it would be inappropriate to state that the region delimited by the points inside the envelope corresponds to the unstable case.

the points inside the envelope corresponds to the unstable case.

Let γ_0 and γ_1 be the minimum and maximum real values of the points along the envelope, respectively. Three cases are possible:

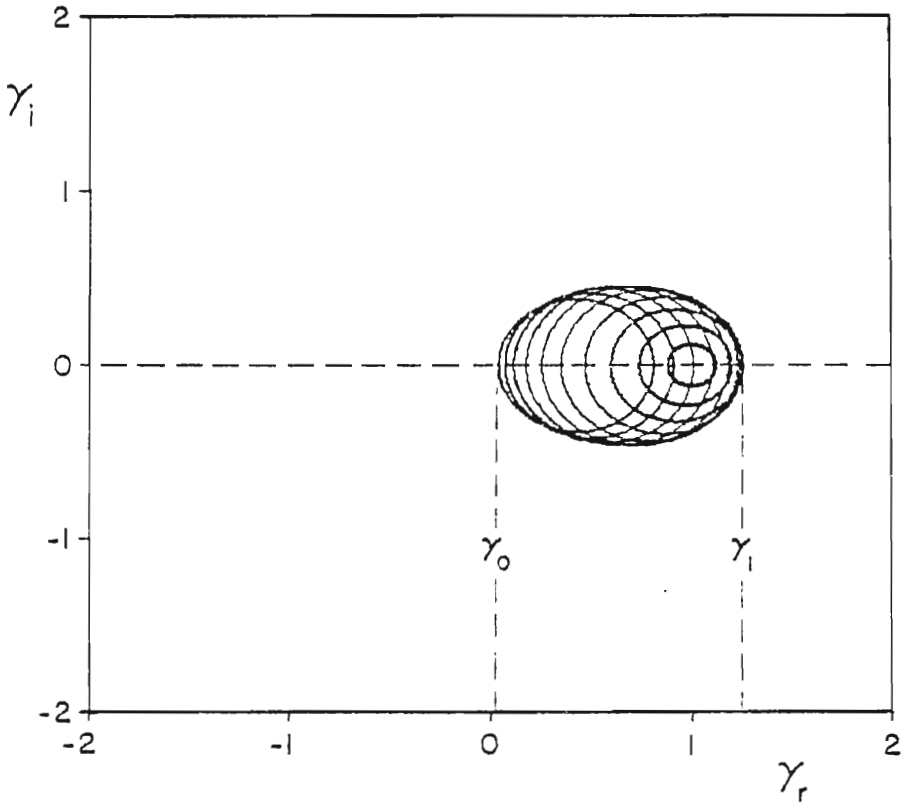

Figure 18. Circumference of equation $|\gamma_r - \mu|^2 + \gamma^2_I = \Phi^2$ in the complex γ plane for $|\eta| \leq 1$.

$$(i)\quad 0<\gamma_0<\gamma_1 \tag{B-20a}$$

$$(ii)\quad \gamma_0<\gamma_1<0 \tag{B-20b}$$

$$(iii)\quad \gamma_0<0<\gamma_1 \tag{B-20c}$$

(i) If both γ_0 and γ_1 are positive, the stability in the χ complex plane corresponds to the points outside the interval (χ_1, χ_0) since the dimensionless frequency k is positive and real (Fig. 19a). (ii) The same result holds if both extremes, γ_0 and γ_1, are negative (Fig. 19b). (iii) If γ_0 is negative and γ_1 is positive, the stability region is determined by the points inside the interval (χ_0, χ_1) (Fig. 19c).

For h_{oo} = 100 m, Δh = 10 m, L_y = 10 km, γ_0 and γ_1 are found to be 0 and 1.25 m sec^{-1}, respectively. For a two-day period, these values correspond to a wavelength less than 21.6 kms. Thus a sufficient condition of stability for a typical upper oceanic front is established. This criterion guarantees that waves whose wavelength are larger than 22 kms may be barotropically stable.

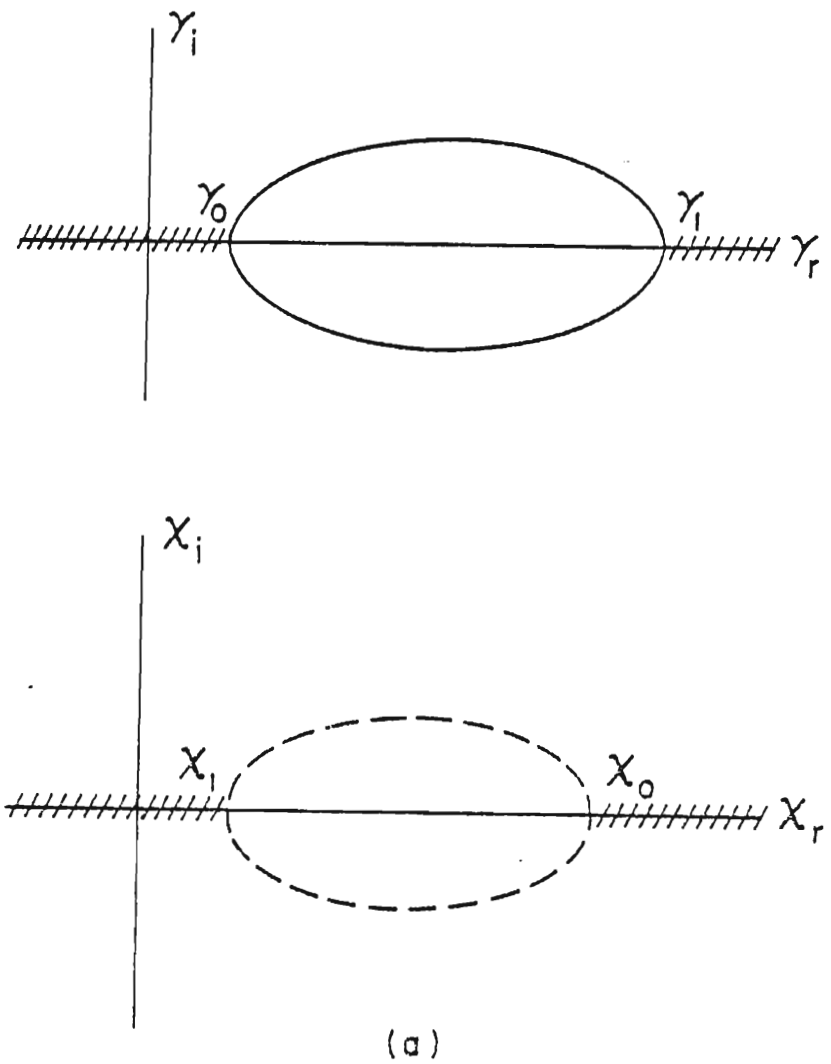

Figure 19. Region of stability in the x complex plane whenever a) γ_0 and γ_1 are positive, b) γ_0 and γ_1 are negative, c) γ_0 is negative and γ_1 is positive.

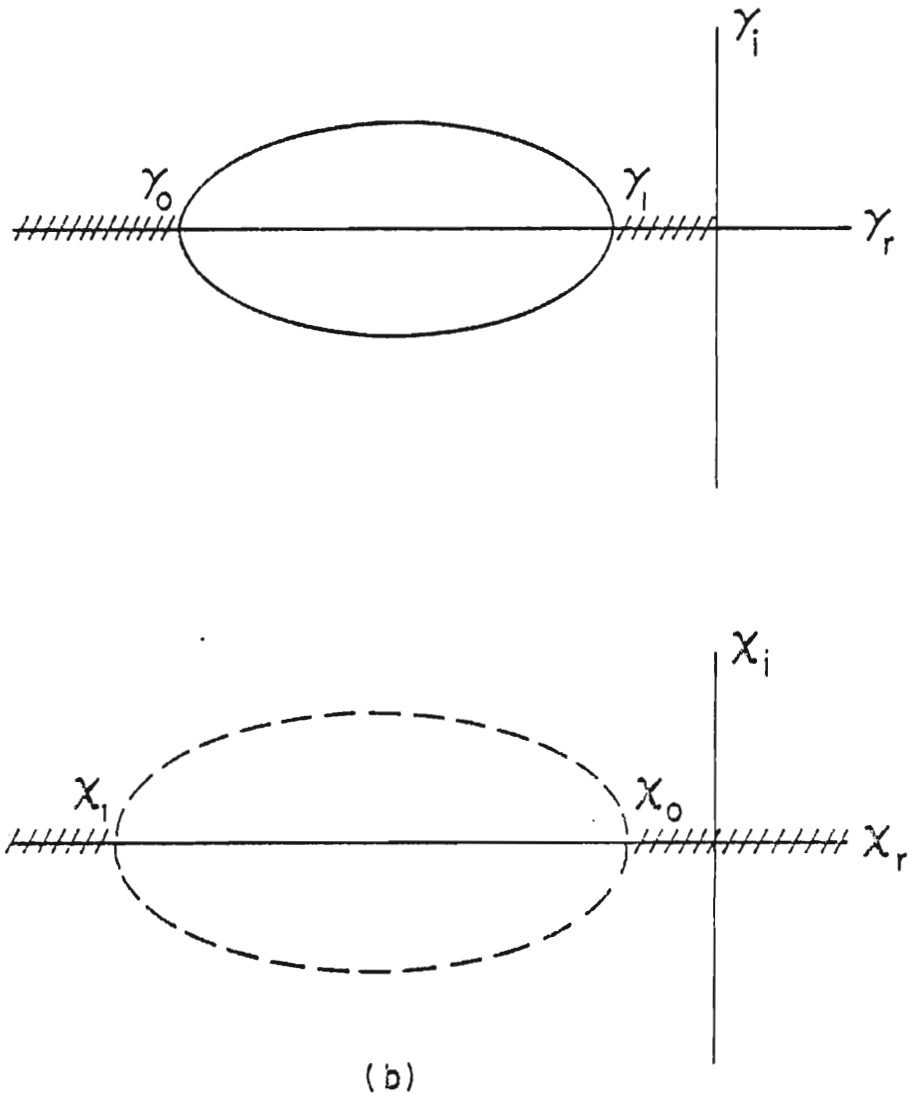

(b)

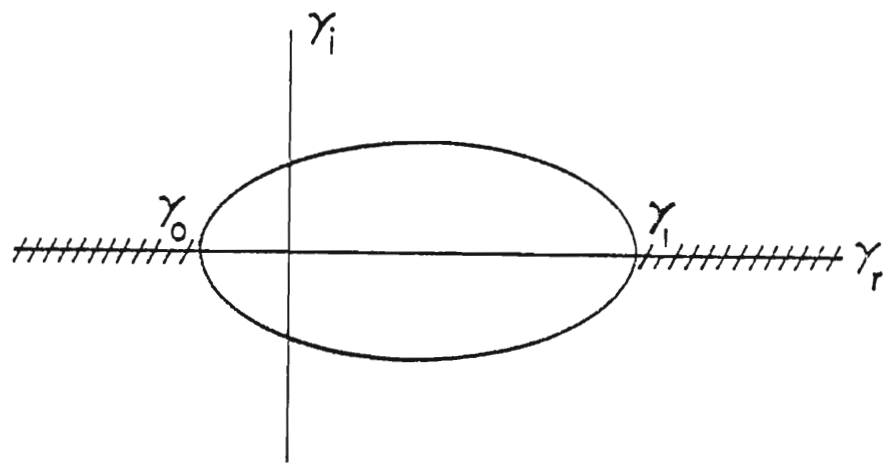

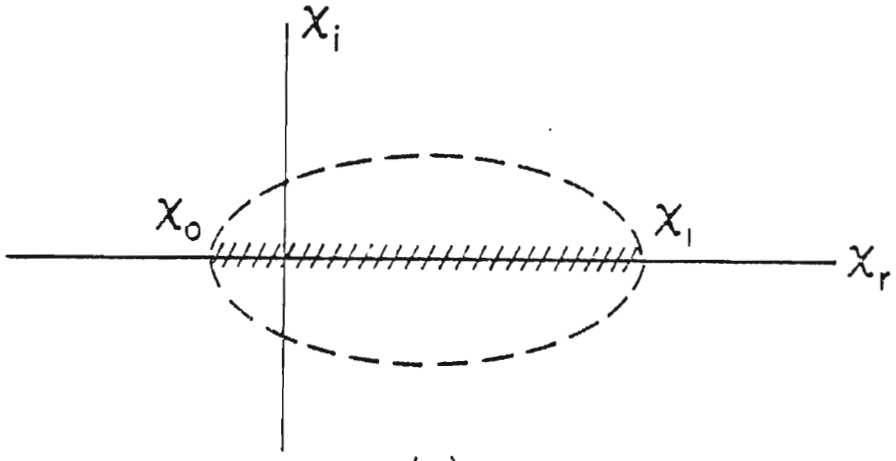

(c)

C. LIST OF SYMBOLS

a	coefficient of thermal expansion
A	horizontal diffusion coefficient of momentum
b	coefficient of saline contraction
B	positive constant defined by Eq. (15b)
c_1, c_2	arbitrary constants, defined by Eq. (54)
c_r, c_i	real and imaginary parts of the phase speed
c	phase speed
C_D	surface drag coefficient
D	depth variation of the first interface
Do	amplitude of the depth variation of the first interface
E	Ekman number
f	Coriolis parameter
F(y)	left hand side of Eq. (45a)
g	gravity acceleration
g*	reduced gravity
G(y)	left hand side of Eq. (45b)
h	thickness
H	mean height
k:	zonal wavenumber
K	positive constant, defined by Eq. (26)
l:	meridional wavenumber
l:	meridional wavenumber
L_x, L_y	latitudinal and meridional frontal length scales

M_{kj}, N_{kj} matrices of elements (k, j) defined by Eqs. (A-7) and (A-12), respectively

p pressure

Pa atmospheric pressure

Q function defined by Eq. (B-9)

r cyclone's radii

r_o, v_o positive constants, defined by Eq. (23)

R positive constant, defined by Eq. (B-12)

Ro thermal Rossby number

S velocity of translation of the cyclone

S salinity

t time

T time scale of dissipation

T temperature

T_0, T_1 positive constant amplitudes of the wind stress, defined by Equations (22) and (25), respectively

u zonal velocity component

v merdional velocity component

V meridional mass transport

V_c, V_p general and particular solutions of the meridional mass transport, V

W width of the basin

X constant defined by Eq. (20)

z independent vertical coordinate, increasing upward

Z function defined by Eq. (B-9)

z independent vertical coordinate, increasing upward

α inverse of the Rossby radius of deformation

β	Coriolis parameter
$\gamma, \eta, \mu, \kappa, \chi$	non-dimensional variables, defined by the system (B-15)
δ	free surface of the uppermost layer
Δh	amplitude of the interfaces' depth variation
Δh	bump height
ΔH	upwelling amplitude
ΔT	temperature amplitude
ε	angle formed by the upwelling and the southward drift of the oceanic front
θ	angle defined by Equations (22a and 22b) respectively
λ	zonal wavelength
ν	maximum value of the pair (i, j)
ρa	air density
$\rho j, \rho o$	sea density
σ	eigenvalue
τ^x, τ^y	horizontal wind stress components
υ	circumferential velocity of the cyclone
T	e-folding time scale
χ, ζ	arbitrary functions defined by Eq. (55)
ψ	phase
Ψ	forcing function defined by Eq. (57)
ω	frequency

REFERENCES

Abramov, A. A., B. A. Tareyev, V. I. Ulyanova, 1972: Baroclinic Instability in Kochin's Two layered Model of a Frontal Wave on a Beta Plane. *Izvestia, Atmos. Oceanic Physics.* Series 8 (2), 79-84.

Bergeron, T., 1928: Über die drei dimensional verknüpfende Wettranalyse I. *Geofys. Publikasjoner,* 5, No. 6, 1-111.

Bjerkness, J., 1919: On the Structure of Moving Cyclones. *Geofys. Publikasjoner,* 1, No. 2.

Black, P. G., and G. Whitee, 1976: The Effect of Hurricane Eloise on the Gulf of Mexico. *Proc. Second Conf. Ocean - Atmosphere Interaction, Seattle, Amer. Meteor. Soc.* Abstracts in *Bull. Amer. Meteor. Soc.,* 57, 139.

Bleck, R., 1973: Numerical Forecasting Experiments Based on the Conservation of Potential Vorticity on Isentropic Surfaces. *J. Applied Meteor.,* 12, 737-752.

_____, 1978: Simulation of Coastal Upwelling Frontogenesis with an Isopycnic Coordinate System. *J. Geophys. Res.,* 83, 6163-6172.

Chang, S. W., and R. A. Anthes, 1978: Numerical Simulations of the Ocean's Nonlinear, Baroclinic Response to Translating Cyclones. *J. Phys. Oceanogr.,* 8, 468-480.

Elliassen, A., and E. Raustein, 1970: A Numerical Integration Experiment with a six-level Atmospheric Model with Isentropic in Formation Surface. *Meteor. Annaler,* 5, 429-449.

Garvine, R. W., 1974: Dynamics of Small-Scale Oceanic Fronts. *J. Phys. Oceanogr.,* 4, 557-569.

_____, 1979: An Integral, Hydro-dynamic Model of Upper Ocean Frontal Dynamics. *J. Phys. Oceanogr.,* 9, 1-36.

Geisler, J. E., 1970: Linear Theory of the Response of a Two Layer Ocean to a Moving Hurricane. *Geophys. Fluid Dyn.,* 1, 249-272.

Hoskins, B. J., 1971: Atmospheric Frontogenesis Models; Some Solutions. *Quart. J. Roy. Met. Soc.,* 97, 139-153.

Hoskins, B. J., 1971: Atmospheric Frontogenesis Models; Some Solutions. *Quart. J. Roy. Met. Soc.,* 97, 139-153.

_____, 1972: Non-Boussinesq Effects and Further Development in a Model of Upper Tropospheric Frontogenesis. *Quart. J. Roy. Met. Soc.,* 98, 532-541.

_____, and F. P. Bretherton, 1972: Atmospheric Frontogenesis Models: Mathematical Formulation and Solution. *J. Atmos. Sci.*, 29, 11-37.

Howard, L. N., 1961: Note on a Paper of John W. Miles. *J. Fluid Mechanics*, 10, 509-512.

Jordan, C. L., 1964: On the Influence of Tropical Cyclones on the Sea Surface Temperature Field. *Proc. Symp. Trop. Meteor., New Zealand Meteor. Service, Wellington*, 614-622.

Kao, T. W., 1980: The Dynamics of Oceanic Fronts. Part I: The Gulf Stream. *J. Phys. Oceanogr.*, 10, 483-492.

Kuo, H. L., 1949: Dynamical Instability of Two-dimensional Nondivergent Flow in a Barotropic Atmosphere. *J. Meteor.*, 6, 105-122.

Leipper, D. F., 1967. Observed Ocean Conditions and Hurricane Hilda, 1964. *J. Atmos. Sci.*, 24, 182-196.

McNider, R. T., and J. J. O'Brien, 1973: A Multi-layer Transient Model of Coastal Upwelling. *J. Phys. Oceanogr.*, 3, 258-273.

MacVean, M. K., and J. R. Woods, 1980: Redistribution of Scalars during Upper Ocean Frontogenesis: a Numerical Model. *Quart. J. Roy. Met. Soc.*, 106, 293-311.

O'Brien, J. J., and R. O. Reid, 1967: The Non-linear Response of a Two-layer, Baroclinic Ocean to a Stationary, Axially-symmetric Hurricane: Part I: Upwelling Induced by Momentum Transfer. *J. Atmos. Sci.*, 24, 208-215.

Orlanski, I., 1968: Instability of Frontal Waves. *J. Atmos. Sci.*, 25, 178-200.

Rayleigh, Lord, 1880: On the Stability or Instability of Certain Fluid Motions. Scientific Papers, Vol. 3, Cambridge University Press, 594-596.

Reed, R., 1955: A Study of a Characteristic Type of Upper Level Frontogenesis. *J. Meteor.*, 12, 226-237.

_____, and F. Sanders, 1953: An Investigation of the Development of a Mid Tropospheric Frontal Zone and Its Associated Vorticity Field, *J. Meteor.*, 10, 338-349.

Roden, G. I., 1970: Aspects of the Mid-Pacific Transition Zone. *J. Geophys. Res.*, 67, 3177-3180.

Roden, G. I., 1970: Aspects of the Mid-Pacific Transition Zone. *J. Geophys. Res.*, 67, 3177-3180.

_____, 1972: Temperature and Salinity Fronts at the Boundaries of the Subarctic - Subtropical Transition Zone in the Western Pacific. *J. Geophys. Res.*, 77, 7175-7187.

_____, 1974: Thermohaline Structure, Fronts, and Sea-Air Energy Exchange of the Trade Wind Region East of Hawaii. *J. Phys. Oceanogr.*, 4, 168-182.

_____, 1975: On North Pacific Temperature, Salinity, Sound Velocity and Density Fronts and their Relation to the Wind and Energy Flux Fields. *J. Phys. Oceanogr.*, 5, 557-571.

_____, 1976: On the Structure and Prediction of Oceanic Fronts. *Naval Research Reviews*, 29, 18-35.

_____, 1977: Oceanic Subarctic Fronts of the Central Pacific: Structure of and Response to Atmospheric Forcing. *J. Phys. Oceanogr.*, 7, 761-778.

_____, 1980: On the Variability of Surface Temperature Fronts in the Western Pacific, as Detected by Satellite. *J. Geophys. Res.*, 85, 2704-2710.

Sanders, F., 1955: Investigation of the Structure and Dynamics of an Intense Surface Frontal Zone. *J. Meteor.*, 12, 542-552.

Shapiro, M. A., 1975: Simulation of Upper-level Frontogenesis with a 20-level Isentropic Coordinate Primitive Equation Model. *Mon. Wea. Rev.*, 103, 591-604.

Suginohara, N., 1973: Response of a Two-layer Ocean to Typhoon Passage in the Western Boundary Region. *J. Oceanogr. Soc. Japan*, 29, 236-250.

Tareyev, B. A., 1968: Non-geostrophic Disturbances and Baroclinic Instability in Two Layered Oceanic Flow. *Izvestia, Atmospheric and Oceanic Physics*, Vol. 14, No. 12, 1275-1284.